Big Data and Information Analytics

https://www.aimspress.com/journal/BDIA

BDIA, 10: 130–157.
DOI:10.3934/bdia.2026007
Received: 21 April 2026
Revised: 25 June 2026
Accepted: 09 July 2026
Published: 29 July 2026

Research article

Advanced modeling approach to percolation on lattices: analysis of complex systems and their implications

Muhammad Imran Shahid*

School of Mathematics and Statistics, Zhengzhou University, Zhengzhou 450001, China

* **Correspondence:** Email: imranzzu87@gmail.com.

Abstract: This research addresses the challenge of three types of non-uniform site percolation on a non-regular Bethe lattice (TNRBL) with its epidemiological implications. By utilizing a non-regular Bethe lattice (NRBL), we explore the estimation of vital percolating variables such as cluster size distribution (CSD), critical connection probability (CCP), percolation probability of connected sites (PP), and average cluster size (ACS). We apply the generating function (GF) and the generalized recursive method (GRM) to gain insights into these variables. The study demonstrates that spanning non-uniform dynamic percolation through the fitted model probabilities enhances the efficiency of intervention strategies, potentially revolutionizing disease control. The findings revealed that, for inhomogeneous site non-uniform percolation on the proposed model, a higher fraction of connection and distribution probabilities enhances the intensity of the percolation process. This increase subsequently leads to a significant enlargement of the mean degree of the system during the percolation process. The shape profiles of the findings are illustrated to observe their behavior across varying parameter choices. Furthermore, we investigated the novel coronavirus 2019 (COVID-19) diffusion pattern utilizing the proposed dynamically altered parameters and identified various variables (courtesy of groups) for disease control methods. We acknowledge that the research being carried out is substantial, that its findings are intended to generate enthusiasm, and that scientists anticipate employing several percolation methods to conduct it. In addition, the research not only adds to the development of more accurate control plans for future global health crises, but it also offers up new avenues for the improvement of models that anticipate epidemics. This study lays the door for an improved comprehension of the complex dynamics of epidemics, and it provides a platform for future studies to investigate a variety of intervention techniques.

Keywords: non-uniform percolation; critical connection probability; TNRBL; average cluster length; COVID-19

Abbreviations: TNRBL: three type non-regular Bethe lattice; CSD: cluster size distribution; CCP:

critical connection probability; APC: average proportion of connectivity; PP: percolation probability; ACS: average cluster size; CPs: connection probabilities; GF: generating function; CP: critical-phase; SCP1: sub-critical phase; SCP2: super-critical phase; NRBL: non-regular Bethe lattice; GRM: generalized recursive method; COVID-19: coronavirus 2019; WHO: World Health Organization.

1. Introduction

In modeling spurious media connections, percolation is a robust statistical mechanics methodology. Statistical mechanics' significantly unambiguous fundamental paradigm similarly illustrates phase transitions demonstrated by the manifestation of a substantial linked component. It is difficult to overstate the theoretical importance of comprehending percolation, fractals, and scaling in such a wide field range, including physics, biology, geophysics, and more. For example, oil recovery, the signaling robustness pathways, and potential molecular remedy targets are all of practical importance and are addressed via the following authors [1]. To forecast chemical, physical, pharmacological, and biological qualities, topological indies have been established [2] and crucial phenomena with a wide range of applications [3]. Percolation happens when the bonds or else sites concerning an aligned lattice are filled independently and probabilistic with a likelihood "p", in addition to a symmetrical phase transition happening with the infinite linked cluster development when "p" is raised beyond a critical threshold p_c. A collection of CEs analogous to an unlikely fractal and ascending structure, as regards their geometric aspects, describes critical phenomena and percolation methodologies serve as significant universality groups in these phenomena. The spin superconductivity transition, SU_3 lattice gauge theory, retention capacity and watersheds of landscapes, and spin quantum Hall transition. Percolation is intriguing from a mathematical perspective because it shows connections between graphs' probabilistic and algebraic/topological characteristics. Despite the fact that the topic has seen a lot of studies, many issues remain unresolved.

Substantially, the researchers, specifically [4] enlarged on [4] illustrating that the most critical site for lattice percolation is limited via a con-formally inflexible scaling constrain as the align associated with the lattice approaches zero. Conversely, the SLE technique permits the overlap of distinct cluster (group) interfaces. As an illustration, the investigators [4] evolved on the SLE6 through incredible [5] by clarifying the previously established significant exponent. After this discovery, other scientists continued to use the CEs for heterogeneous percolation. Reference [6] was the initial scientific study to find heterogeneous percolation. Theorists have initiated inquiries into this specific type of percolation to investigate the impact of sites or bonds on occupancy probability. Reference [7] expanded the claim related to [8] by utilizing heterogeneous percolation (bond) by using numerous lattice types via paradigm, according to reference towards the crossings box-idea. Turban [9] figured out a 2D bound percolation issue regarding Bethe lattice circumstances utilizing the ghost site approach. Typically, inhomogeneous percolation occurs upon regular lattices adjacent to the diverse site neighbors, resulting in real-world problems [10–15]. There have already been certain instances when abrupt or discontinuous percolation transitions (explosives) were observed, that examines the behavior of multilayer networks in statistical mechanics and percolation theory [16].

Continuing the scholars employed CEs on the UBL to investigate numerous dynamical dimensions surrounding problems from the real world. The study's authors [17–25] have established precisely the goals intended to acquire the various percolating variates. We acquired concerning the functioning numerous variables around the phase transitions associated with CEs for 3D-ADCM [22]. The COVID-19 dispersion requires thoughtful consideration during the percolation process. Numerous scientists might be enabled to associate filled sites through the lattice (Bethe) for amplified individuals, as well as techniques On behalf of their movement and likely infections among persons, by implementing the resulting generalization of the obstacles to the circumstance surrounding epidemic transmission [22, 23, 26–30]. Regrading the inhomogeneous percolation theory presents an innovative theoretical framework for optimizing public health governance interventions, developed from network/lattice theory [31–35].

The execution of a lattice paradigm to depict disease transmission and resource allocation signifies the simulation of complex links between individuals, surrounding circumstances, and treatments. The lattice is a sequential structure in which each node represents a person or a collection of individuals. The connections between nodes represent potential paths around disease transmission and intervention [36–40]. This technique improves the efficiency of determining critical thresholds during public health policies, which enabled policymakers to prioritize schemes that address the most vulnerable or interlinked groups. Implementing heterogeneous percolation principle in public health governance could contribute to more optimal resource allocation as well as promptly interventions [41–45]. As a result, information handling develops into more complex, rendering easy resolution unfeasible. As a matter of fact, we devised a manner alongside such a problematic situation, which will need advanced CEs.

Building on earlier studies of inhomogeneous percolation on irregular lattice structures [23], the present work introduces a parameterized TNRBL. The main novelty of this study lies in treating site-type distribution, coordination number, and connection probability as coupled parameters that jointly control cluster formation and network connectivity. From a physics point of view, this formulation represents a disordered connectivity system in which local structural heterogeneity affects the formation, growth, and stability of connected clusters. The proposed TNRBL model allows the connectivity behavior of complex systems to be examined through key quantities, including CSD, CCP, PP and ACS. These quantities describe the formation of finite clusters, the variation of connectivity with connection probability, and the likelihood of developing system-level connected clusters under heterogeneous lattice conditions. The epidemic application further shows how heterogeneous infection probabilities, contact patterns, and population structures influence the growth of local infection clusters and the risk of wider disease spread. Therefore, the present study provides an analytical extension of non-uniform percolation modeling and a quantitative framework for analyzing connectivity growth in complex epidemic systems.

The structure of the paper is as follows: Section 2 presents the basic description of the proposed methodology; Section 3 presents the numerous distinct formulations regarding the proposed methodology; Section 4 reveals the sensitivity analysis aspect of the proposed strategy; Section 5 our investigation reveals the epidemiological application; and the paper concludes in Section 6.

2. Suggested framework

In the current investigation, the suggested strategy is an NRBL with three distinct *ii*d (Identically and independently distributed) sites. An NRBL is a lattice where sites have varying numbers of neighbors, unlike a regular Bethe lattice where each site has the same number of neighbors.

Percolation, as we perceive it, is the random connectivity of sites on the lattice, also called site percolation. It is one of the most prominent aspects of explaining the crucial mechanisms of complex structures. In non-uniform percolation, the sites have diverse coordination numbers and unique connection probabilities, leading to a more complex percolation process. The utility of our method is that any Bethe lattice site is connected via a *ii*d, a 3-site distribution; additionally, such sites are connected on three kinds.

The Figure 1 depicts the structural mechanism for TNRBL in non-uniform percolation. The NRBL, denoted as $NRBL(\mathbf{z}, \boldsymbol{\alpha})$, is a hierarchical tree-like structure characterized by non-uniform sites with the vector of coordination number $\mathbf{z}$ and site distribution probability $\boldsymbol{\alpha}$. Extending this framework, the TNRBL introduces a percolation scheme governed by connection probabilities $p_i = \lambda_i/k_i$ $\left(p_1 = \left(\frac{\lambda_1}{k_1}\right),\ p_2 = \left(\frac{\lambda_2}{k_2}\right),\ \text{and}\ p_3 = \left(\frac{\lambda_3}{l-k_1-k_2}\right)\right)$, where λ_i is the average proportion of connectivity (APC) for site type i, and k_i represents the number of connected sites of type i. To maintain valid probabilities ($0 \le p_i \le 1$), constraints $\lambda_i \le k_i$ are enforced. The basic mechanism of our approach is comprised of 3-variables (vector): the connection probability (CP), coordination number (CN), along with the distribution probability (DP). The basic illustration of the Figure 1 is that the structural algorithm is utilized to realize TNRBL for the single realization $\left\{\frac{\boldsymbol{\lambda}}{\mathbf{k}}; \mathbf{z}, \boldsymbol{\alpha}\right\}$. Here, the CN concerning the first kind of site (shown by a triangle), the second kind of site (represented by a square), and the third type site (illustrated by a pentagon) are 3, 4 and 5, respectively, with varying site DP associated with 0.25, 0.33 and 0.42. Different kinds of clusters of different sizes have been developed for every possible TNRBL realization.

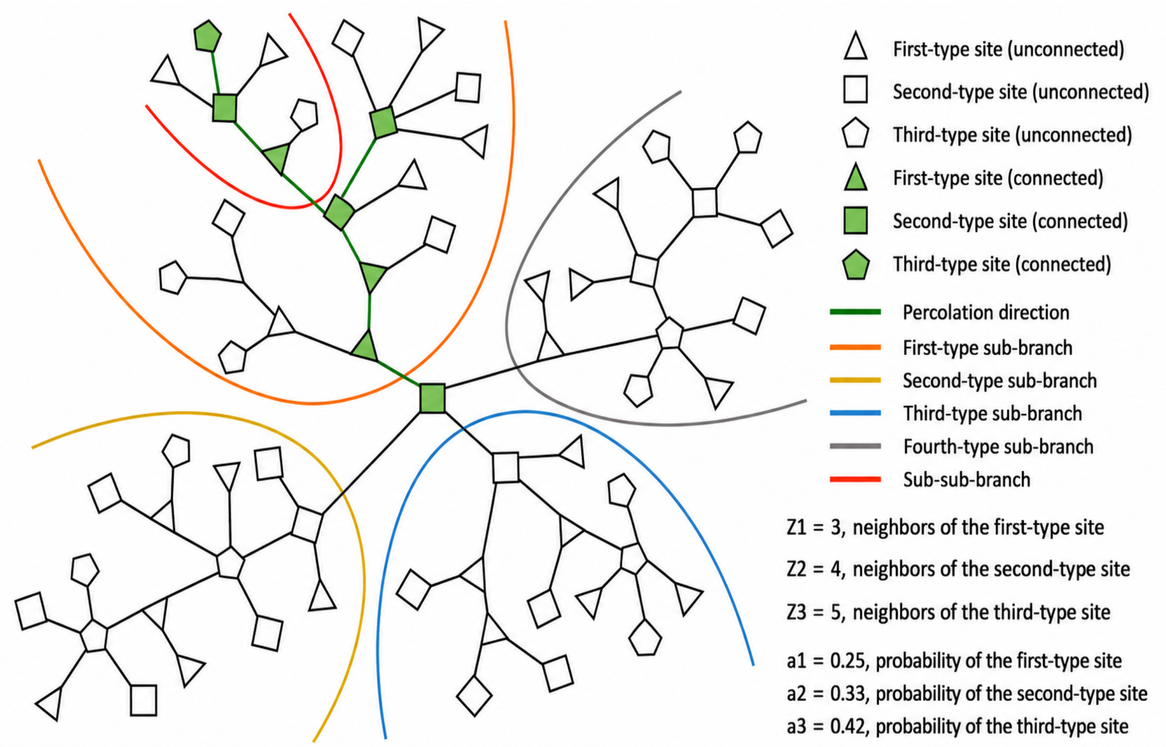

Figure 1. The structural mechanism for TNRBL in the process of non-uniform percolation.

3. Non-uniform percolation inquiry on TNRBL

3.1. Cluster size distribution of connected sites

In this subsection, we analyze the structural factors affecting the CSD and provide a consistent expression for its mathematical form. During the percolation process, finite clusters of different sizes can be generated, while the emergence of an infinite or spanning cluster represents the onset of global connectivity. In the proposed TNRBL framework, the cluster size is denoted by l, whereas the perimeter size, denoted by t, represents the number of unconnected boundary sites required to isolate a finite cluster from the surrounding lattice. Let k_i denote the number of type-i sites in an l-cluster, where $k_1 + k_2 + k_3 = l$. The coordination number of a type-i site is denoted by z_i. Therefore, before the internal cluster connections are formed, the total number of available connectivity stubs in an l-cluster is $\sum_{i=1}^{3} k_i z_i$. Unlike an ordinary Bethe lattice, where each internal connection consumes two connectivity stubs, the proposed TNRBL is constructed through a three-directional connectivity rule. In this framework, each internal connection removes three effective connectivity stubs from the cluster perimeter. Since a finite tree-like cluster of size l contains $l - 1$ internal connections, the perimeter size is expressed as

$$t = \sum_{i=1}^{3} k_i z_i - 3(l-1) = \sum_{i=1}^{3} k_i z_i - 3l + 3 = 3 + \sum_{i=1}^{3} k_i (z_i - 3). \tag{3.1}$$

Equation (3.1) provides the effective perimeter size of an l-cluster in the TNRBL model. This expression is model-specific and reflects the three-directional connectivity mechanism of the proposed lattice. It also provides the mathematical basis for the appearance of the exponent 3 and the term $z_i - 3$ in the final CSD expression. Let a_i denote the occurrence probability of a type-i site, satisfying $\sum_{i=1}^{3} a_i = 1$. The connection probability of a type-i site is defined via $p_i = \frac{\lambda_i}{\kappa_i}$, where λ_i is the average number of connected neighbors of a type-i site and κ_i is the corresponding connectivity capacity. For the present TNRBL, κ_i can be taken as the coordination number z_i. The average connection probability of the heterogeneous lattice is then $\bar{p} = \sum_{i=1}^{3} a_i p_i = \sum_{i=1}^{3} a_i \frac{\lambda_i}{\kappa_i}$. Consider $A(l, \boldsymbol{\lambda}/\boldsymbol{\kappa})$ as the event that a randomly selected site belongs to a finite cluster of size l. For a fixed cluster composition $\mathbf{k} = (k_1, k_2, k_3)$, the probability contribution consists of the structural factor b_l, the multinomial arrangement of the three site types, the probability that the l sites are connected, and the probability that the t perimeter sites remain unconnected. Thus,

$$P\left(A\left(l, \frac{\boldsymbol{\lambda}}{\boldsymbol{\kappa}}\right) \mid \mathbf{k}\right) = b_l \binom{l}{k_1, k_2, k_3} \prod_{i=1}^{3} \left(a_i \frac{\lambda_i}{\kappa_i}\right)^{k_i} (1 - \bar{p})^t, \tag{3.2}$$

substituting the perimeter expression from Eq (3.1) into Eq (3.2), are given via

$$P\left(A\left(l, \frac{\boldsymbol{\lambda}}{\boldsymbol{\kappa}}\right) \mid \mathbf{k}\right) = b_l \binom{l}{k_1, k_2, k_3} \prod_{i=1}^{3} \left(a_i \frac{\lambda_i}{\kappa_i}\right)^{k_i} (1 - \bar{p})^{3 + \sum_{i=1}^{3} k_i (z_i - 3)},$$

$$(1 - \bar{p})^{3 + \sum_{i=1}^{3} k_i (z_i - 3)} = (1 - \bar{p})^3 \prod_{i=1}^{3} (1 - \bar{p})^{k_i (z_i - 3)},$$

$$P\left(A\left(l, \frac{\boldsymbol{\lambda}}{\boldsymbol{\kappa}}\right) \mid \mathbf{k}\right) = b_l(1-\bar{p})^3 \binom{l}{k_1, k_2, k_3} \prod_{i=1}^{3} \left[a_i \frac{\lambda_i}{\kappa_i} (1-\bar{p})^{z_i-3} \right]^{k_i}. \tag{3.3}$$

Equation (3.3) shows that the probability of an l-cluster is governed by the connected-site probabilities and the unconnected perimeter contribution. The factor $(1 - \bar{p})^3$ arises from the three-directional boundary correction of the TNRBL, whereas the term $(1 - \bar{p})^{z_i-3}$ represents the remaining unconnected perimeter contribution associated with a type-i site. Finally, summing Eq (3.3) over all possible compositions satisfying $k_1 + k_2 + k_3 = l$, and using the multinomial theorem, gives

$$P\left(A\left(l, \frac{\boldsymbol{\lambda}}{\boldsymbol{\kappa}}\right)\right) = b_l(1-\bar{p})^3 \sum_{k_1+k_2+k_3=l} \binom{l}{k_1, k_2, k_3} \prod_{i=1}^{3} \left[a_i \frac{\lambda_i}{\kappa_i} (1-\bar{p})^{z_i-3} \right]^{k_i},$$

$$P\left(A\left(l, \frac{\boldsymbol{\lambda}}{\boldsymbol{\kappa}}\right)\right) = b_l \left(1 - \sum_{i=1}^{3} a_i \frac{\lambda_i}{\kappa_i}\right)^3 \left[\sum_{i=1}^{3} a_i \frac{\lambda_i}{\kappa_i} \left(1 - \sum_{j=1}^{3} a_j \frac{\lambda_j}{\kappa_j}\right)^{z_i-3} \right]^l. \tag{3.4}$$

Since $\bar{p} = \sum_{i=1}^{3} a_i \frac{\lambda_i}{\kappa_i}$, the cluster size distribution can be expressed as Eq (3.4). Equation (3.4) gives the probability that a randomly selected site belongs to an l-cluster in the proposed TNRBL. The term b_l represents the number of possible l-cluster configurations with different geometric structures. However, due to the spatial-geometric complexity of clusters in the heterogeneous lattice, direct enumeration of b_l is difficult. Therefore, the generating function approach is adopted in the next subsection to evaluate the percolation probability of connected sites.

3.2. Percolation probability of connected sites

The observable cluster does not demonstrate the trait of crossing the NRBL on its sides, a behavior often found in clusters with insignificant connection probabilities. Perceive $E(\mathbf{p}) = \left(\frac{\boldsymbol{\lambda}}{\mathbf{k}}\right)$ which represents the random event that occurs when the site corresponds to the large cluster, and $E\left(\frac{\boldsymbol{\lambda}}{\mathbf{k}}\right)$ to be the arbitrary event (APC) in which the site belongs to the measurable cluster due to the structural mechanism of NRBL. We might determine the probability that an event belongs to an extensive large cluster via the likely outcome theorem, which is an additional rule of probability regarding disconnected occurrences, is given by

$$\begin{aligned} P\left(E\left(\frac{\boldsymbol{\lambda}}{\mathbf{k}}\right)\right) &= \sum_{l=1}^{\infty} P\left(A\left(l, \frac{\boldsymbol{\lambda}}{\mathbf{k}}\right)\right), \\ &= \left(1 - \sum_{i=1}^{3} a_i \frac{\lambda_i}{k_i}\right)^3 \sum_{l=1}^{\infty} l b_l \left(\sum_{i=1}^{3} a_i \frac{\lambda_i}{k_i} (1-\overline{p})^{z_i-3}\right)^l, \end{aligned} \tag{3.5}$$

for ($i = 1, 2, 3$) and ($l = 1, 2, ...\infty$). We need to quantify the CCP based on the percolation process. As a result, we require a power series $f(x) = \sum_{l=1}^{\infty} b_l x^l$ that is utterly convergent, and indeed the formulation for the GF is provided via

$$d(x, y) = y^3 \sum_{l=1}^{\infty} l b_l x^l = y^3 x f'(x), \tag{3.6}$$

the Eq (3.6) holds under the following scenario, in which the power series $f(x)$ is convergent, for further explanation of the second equality of Eq (3.6). Again for conditions in the Eq (3.6), substitute the following ones. $x\left(\frac{\boldsymbol{\lambda}}{\mathbf{k}}\right) = \sum_{i=1}^{3} a_i \frac{\lambda_i}{k_i} \left((1-\overline{p})^{z_i-3}\right)^l$ and $y\left(\frac{\boldsymbol{\lambda}}{\mathbf{k}}\right) = \left(1 - \sum_{i=1}^{3} a_i \frac{\lambda_i}{k_i}\right)^3$. In this instance, the GF is represented as $x\left(\frac{\boldsymbol{\lambda}}{\mathbf{k}}\right)$ and the expression $y\left(\frac{\boldsymbol{\lambda}}{\mathbf{k}}\right)$ is additionally a GF. We are limited to $x\left(\frac{\boldsymbol{\lambda}}{\mathbf{k}}\right) \geq 0$ due to $\left(\frac{\boldsymbol{\lambda}}{\mathbf{k}}\right) \in [0,1]^3$. Similar strategies are modeled, including such $x\left(\frac{\boldsymbol{\lambda}}{\mathbf{k}}\right)$. Via equating Eqs (3.5) and (3.6), we obtain the following result

$$P\left(E\left(\frac{\boldsymbol{\lambda}}{\mathbf{k}}\right)\right) = y^3\left(\frac{\boldsymbol{\lambda}}{\mathbf{k}}\right) x\left(\frac{\boldsymbol{\lambda}}{\mathbf{k}}\right) f'\left(x\left(\frac{\boldsymbol{\lambda}}{\mathbf{k}}\right)\right), \tag{3.7}$$

given that $f'\left(x\left(\frac{\boldsymbol{\lambda}}{\mathbf{k}}\right)\right)$ is known, it follows that $P\left(E\left(\frac{\boldsymbol{\lambda}}{\mathbf{k}}\right)\right)$ would be solved. In the Eq (3.6) above, we get the value $f'\left(\sum_{i=1}^{3} a_i \frac{\lambda_i}{k_i}(1-\overline{p})^{z_i-3}\right)$. As a result, we need to study the GF, $\sum_{i=1}^{3} a_i \frac{\lambda_i}{k_i}(1-\overline{p})^{z_i-3}$ using the extremum assumption. Following that, we obtain the following equation for the $f'\left(x\left(\frac{\boldsymbol{\lambda}}{\mathbf{k}}\right)\right)$ about the specific CCP, which is provided as:

$$\frac{\partial(x)}{\partial\left(\lambda_u/k_u\right)} = a_u \left(1 - \sum_{i=1}^{3} a_i \frac{\lambda_i}{k_i}\right)^{z_u-4} \left(1 - \sum_{i=1}^{3} a_i \frac{\lambda_i}{k_i}(z_i-2)\right) = 0, \tag{3.8}$$

for $(u = 1,\ 2,\ 3)$ and $(i = 1,\ 2,\ 3)$. The given formula reflects the differentiation of $x\left(\frac{\boldsymbol{\lambda}}{\mathbf{k}}\right)$ with regard to connection probabilities, where "u" indicates the order of differentiations. We get these points, $1 - \sum_{i=1}^{3} a_i \frac{\lambda_i}{k_i} = 0$ and $\sum_{l=1}^{\infty} a_i \frac{\lambda_i}{k_i}(z_i-2) = 1$. So we see, these points are a function of connection probabilities. Replacing these values into $x\left(\frac{\boldsymbol{\lambda}}{\mathbf{k}}\right) = \sum_{i=1}^{3} a_i \frac{\lambda_i}{k_i}(1 - \sum_{i=1}^{3} a_i \frac{\lambda_i}{k_i})^{z_i-3}$ individually to gain maximum value of CCP. Moreover, if we place $\left(\sum_{i=1}^{3} a_i \frac{\lambda_i}{k_i} = 1\right)$ via $x\left(\frac{\boldsymbol{\lambda}}{\mathbf{k}}\right)$ subsequently $x\left(\frac{\boldsymbol{\lambda}}{\mathbf{k}}\right) = 0$, resulting in the GF $x\left(\frac{\boldsymbol{\lambda}}{\mathbf{k}}\right) \geq 0$, and $\boldsymbol{\lambda} = \mathbf{pk}$, explicitly $\forall\ \mathbf{p} \in [0,1]^3$, and $\boldsymbol{\lambda}$ is the APC vector. As a result, at $\sum_{i=1}^{3} a_i \frac{\lambda_i}{k_i} = 1$ there does not exist a maximum feasible value for GF. On the contrary, GF accomplishes its maximum value at $\sum_{i=1}^{3} a_i \frac{\lambda_i}{k_i}(z_i-2) = 1$, this is the single exclusive significant assessment that follows $x\left(\frac{\boldsymbol{\lambda}}{\mathbf{k}}\right)$. For simplicity, consider the following expression (first part) $\theta\left(\frac{\boldsymbol{\lambda}}{\mathbf{k}}\right) = \sum_{l=1}^{\infty} a_i \frac{\lambda_i}{k_i}(z_i-2)$.

The percolation criterion is a value of $\frac{\boldsymbol{\lambda}}{\mathbf{k}}$ that indicates there is incontestably no longer an uninterrupted connection from one to another side-way. An infinite cluster would not be directly or indirectly associated for trivial sufficient CPs, $\frac{\boldsymbol{\lambda}}{\mathbf{k}}$ in the percolation technique, as well as the cumulative probability that a site belongs to a finite group is equal to the cumulative probability that sites are interconnected. As a result, we have the following expression, which is intended for any sites using the suggested methodology: is in the SCP1, and $P\left(E\left(\frac{\boldsymbol{\lambda}}{\mathbf{k}}\right)\right)$ is approximately equivalent to the $p\left(\frac{\boldsymbol{\lambda}}{\mathbf{k}}\right)$, where the likelihood of a particular site occurring is constrained to $p\left(\frac{\boldsymbol{\lambda}}{\mathbf{k}}\right)$. The following expression $\sum_{i=1}^{3} a_i \frac{\lambda_i}{k_i} = p\left(\frac{\boldsymbol{\lambda}}{\mathbf{k}}\right)$ provides the expectation for the mean-field for the CP. Utilizing the mean field, the corresponding formula is derived. When considering $\frac{\boldsymbol{\lambda}}{\mathbf{k}}$ as a vector, the sub-critical phase (SCP1), super-critical phase (SCP2), and critical phase (CP) of the NRBL are illustrated as $\frac{\boldsymbol{\lambda}}{\mathbf{k}} < \frac{\boldsymbol{\lambda}_c}{\mathbf{k}_c}$, $\frac{\boldsymbol{\lambda}}{\mathbf{k}} = \frac{\boldsymbol{\lambda}_c}{\mathbf{k}_c}$, and $\frac{\boldsymbol{\lambda}}{\mathbf{k}} > \frac{\boldsymbol{\lambda}_c}{\mathbf{k}_c}$, respectively. Additionally, we checked to see if CP is just the maximum implication for the line $x\left(\frac{\boldsymbol{\lambda}}{\mathbf{k}}\right)$. The following result is obtained by applying the finite CP vector result from the Eq (3.7), which is provided by

$$f'\left(x\left(\frac{\boldsymbol{\lambda}}{\mathbf{k}}\right)\right) = \frac{\lambda\left(\frac{\lambda}{\mathbf{k}}\right)}{y^3\left(\frac{\lambda}{\mathbf{k}}\right)x\left(\frac{\lambda}{\mathbf{k}}\right)},$$
$$= \frac{\sum_{i=1}^{3} a_i \frac{\lambda_i}{k_i}}{\left(1-\sum_{i=1}^{3} a_i \frac{\lambda_i}{k_i}\right)^3 \sum_{i=1}^{3} a_i \frac{\lambda_i}{k_i}\left(1-\sum_{i=1}^{3} a_i \frac{\lambda_i}{k_i}\right)^{z_i-3}}, \quad \text{for SCP1.} \tag{3.9}$$

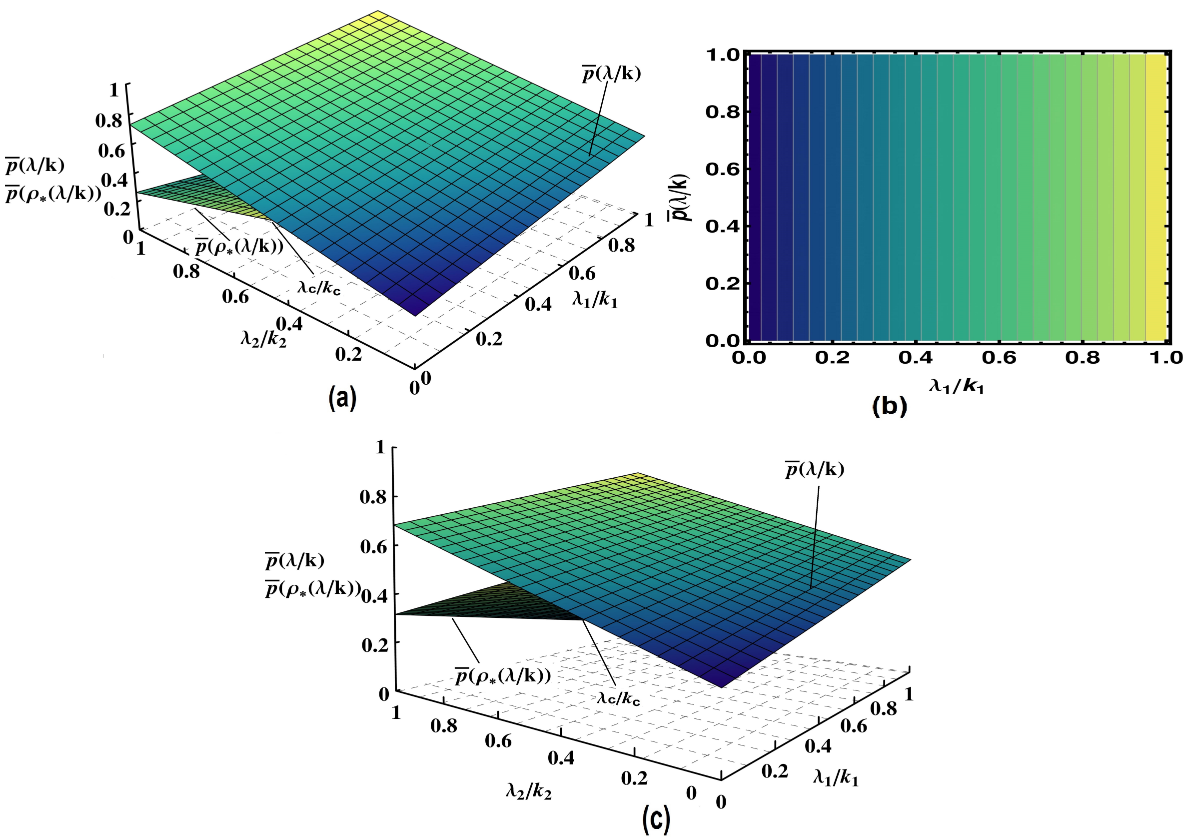

Figure 2. The complementary associations among different variants $\overline{p}\left(\frac{\lambda}{\mathbf{k}}\right)$, $\overline{p}(\rho_*\left(\frac{\lambda}{\mathbf{k}}\right))$, as well as $\frac{\lambda}{\mathbf{k}}$, as suggested approach TNRBL $\left\{\left(\frac{\lambda_1}{k_1}, \frac{\lambda_2}{k_2}, \frac{\lambda_3}{k_3}\right); (3, 4, 5)(0.25, 0.33, 0.42)\right\}$ with $\frac{\lambda_1}{k_1}$ and $\frac{\lambda_2}{k_2}$ at (**a**) $\frac{\lambda_3}{k_3} = 0.40$, (**b**) $\frac{\lambda_2}{k_2} = 0.55$ and $\frac{\lambda_3}{k_3} = 0.60$, and (**c**) $\frac{\lambda_3}{k_3} = 0.60$, which are shown via 2D and 3D figures.

The Eq (3.9) shows the differentiation with respect to $x\left(\frac{\lambda}{\mathbf{k}}\right)$. Next procedure, we shall develop the constraint for all $\boldsymbol{\lambda}/\mathbf{k} \in [0, 1]^3$. From Figure 2(a), If any $\boldsymbol{\lambda}/\mathbf{k} \in [0, 1]^3$, is under $\frac{\lambda}{\mathbf{k}} > \frac{\lambda_c}{\mathbf{k_c}}$ then the existence corresponding value lies in $\frac{\lambda}{\mathbf{k}} < \frac{\lambda_c}{\mathbf{k_c}}$ at $x\left(\frac{\lambda_*}{\mathbf{k}_*}\right) = x\left(\frac{\lambda}{\mathbf{k}}\right)$. Obviously, we acquire the expression for $f'\left(x\left(\frac{\lambda}{\mathbf{k}}\right)\right)$ utterly $\frac{\lambda}{\mathbf{k}} \in [0, 1]^3$, in the case that CP is comparable in the direction of $\theta\left(\frac{\lambda}{\mathbf{k}}\right) = 1$. If that are the cases, then SCP1 and SCP2 signify $\theta\left(\frac{\lambda}{\mathbf{k}}\right) < 1$ and $\theta\left(\frac{\lambda}{\mathbf{k}}\right) > 1$, correspondingly. Afterward the vector $\frac{\lambda}{\mathbf{k}}$ appeases SCP2 as we employ its corresponding value $\boldsymbol{\lambda}_*/\mathbf{k}_*$ which contents $\frac{\boldsymbol{\lambda}_*}{\mathbf{k}_*} < \frac{\boldsymbol{\lambda}_c}{\mathbf{k}_c}$. Establish the mapping ρ_* beyond $[0, 1]^3$, therefore CPs plane via the following

$$\rho_*\left(\frac{\boldsymbol{\lambda}}{\mathbf{k}}\right)=\begin{cases}\frac{\boldsymbol{\lambda}}{\mathbf{k}} & \text{under, } \frac{\boldsymbol{\lambda}}{\mathbf{k}}<\frac{\boldsymbol{\lambda}_c}{\mathbf{k_c}},\\ \frac{\boldsymbol{\lambda}_*}{\mathbf{k}_*} & \text{under, } \frac{\boldsymbol{\lambda}}{\mathbf{k}}>\frac{\boldsymbol{\lambda}_c}{\mathbf{k_c}}.\end{cases} \tag{3.10}$$

So, the expression $\left(\frac{\boldsymbol{\lambda}}{\mathbf{k}}\right)$, explicitly $\forall\ \mathbf{p}\in[0,1]^3$, and $\boldsymbol{\lambda}$ is the APC vector. The mapping converts all vectors toward $\frac{\boldsymbol{\lambda}}{\mathbf{k}}\in[0,1]^3$ based upon the dispersion of the mean mapping of the CPs previously mentioned, in SCP2. For this elucidation of the formulation, which is mean mapping of CPs, explicitly $\forall\ \frac{\boldsymbol{\lambda}}{\mathbf{k}}\in[0,1]^3$, $\rho_*\left(\frac{\boldsymbol{\lambda}}{\mathbf{k}}\right)$ fulfills to $\rho_*(\frac{\boldsymbol{\lambda}}{\mathbf{k}})<\frac{\boldsymbol{\lambda}_c}{\mathbf{k}_c}$. For the purpose of convenience, the equality Eq (3.9), which is stand for $\rho_*\left(\frac{\boldsymbol{\lambda}}{\mathbf{k}}\right)$ which is equal to the $\rho\left(\frac{\boldsymbol{\lambda}}{\mathbf{k}}\right)$, is procured as follows:

$$f'\left(x\left(\frac{\boldsymbol{\lambda}}{\mathbf{k}}\right)\right)=\frac{\sum_{i=1}^{3}a_i\frac{\lambda_i}{k_i}\left(\rho_*\left(\frac{\boldsymbol{\lambda}}{\mathbf{k}}\right)\right)}{\sum_{i=1}^{3}a_i\frac{\lambda_{*i}}{k_{*i}}\left(1-\sum_{i=1}^{3}a_i\frac{\lambda_{*i}}{k_{*i}}(\rho_*\left(\frac{\boldsymbol{\lambda}}{\mathbf{k}}\right))\right)^{z_i}}\ \text{ for } (i=1,\ 2,\ 3), \tag{3.11}$$

under sub critical phase, the Eq (3.11) can be determined. Utilizing Eq (3.11) with scenario Eq (3.4) yields the following for finite CPs; the resultant form is shown by

$$\left(E\left(\frac{\boldsymbol{\lambda}}{\mathbf{k}}\right)\right)=\sum_{i=1}^{3}a_i\frac{\lambda_{*i}}{k_{*i}}\left(\rho_*\left(\frac{\boldsymbol{\lambda}}{\mathbf{k}}\right)\right)\frac{\sum_{i=1}^{3}a_i\frac{\lambda_i}{k_i}\left(1-\sum_{i=1}^{3}a_i\frac{\lambda_i}{k_i}\left(\frac{\boldsymbol{\lambda}}{\mathbf{k}}\right)\right)^{z_i}}{\sum_{i=1}^{3}a_i\frac{\lambda_{*i}}{k_{*i}}\left(1-\sum_{i=1}^{3}a_i\frac{\lambda_{*i}}{k_{*i}}\left(\rho_*\left(\frac{\boldsymbol{\lambda}}{\mathbf{k}}\right)\right)\right)^{z_i}}. \tag{3.12}$$

Therefore, we designed to detect the GF criterion $\left(x\left(\rho_*\left(\frac{\boldsymbol{\lambda}}{\mathbf{k}}\right)\right)=x\left(\frac{\boldsymbol{\lambda}}{\mathbf{k}}\right)\right)$, in addition to GF of $x\left(\frac{\boldsymbol{\lambda}}{\mathbf{k}}\right)$. We contain the significant component of Eq (3.11). Up until recently, the final findings for the probability on average indicating a specific site belongs to an identifiable finite cluster have been written as:

$$P\left(E\left(\frac{\boldsymbol{\lambda}}{\mathbf{k}}\right)\right)=\sum_{i=1}^{3}a_i\frac{\lambda_{*i}}{k_{*i}}\left[\frac{1-\left(a_1\frac{\lambda_1}{k_1}+a_2\frac{\lambda_2}{k_2}+a_3\frac{\lambda_3}{k_3}\right)}{1-\left(a_1\frac{\lambda_{*1}}{k_{*1}}+a_2\frac{\lambda_2}{k_{*2}}+a_3\frac{\lambda_{*3}}{k_{*3}}\right)}\right]^3. \tag{3.13}$$

If we eventually put $\rho_*\left(\frac{\boldsymbol{\lambda}}{\mathbf{k}}\right)=\frac{\boldsymbol{\lambda}}{\mathbf{k}}$, put in Eq (3.13) then we get $P\left(E\left(\frac{\boldsymbol{\lambda}}{\mathbf{k}}\right)\right)$, which is complementary to $\frac{\boldsymbol{\lambda}}{\mathbf{k}}=\frac{\boldsymbol{\lambda}_c}{\mathbf{k_c}}$, for $\frac{\boldsymbol{\lambda}}{\mathbf{k}}<\frac{\boldsymbol{\lambda}_c}{\mathbf{k_c}}$. Furthermore, for $\frac{\boldsymbol{\lambda}}{\mathbf{k}}>\frac{\boldsymbol{\lambda}_c}{\mathbf{k_c}}$, assuming $\rho_*\left(\frac{\boldsymbol{\lambda}}{\mathbf{k}}\right)<\frac{\boldsymbol{\lambda}}{\mathbf{k}}$ is utilized to Eq (3.13), we obtain $P\left(E\left(\frac{\boldsymbol{\lambda}}{\mathbf{k}}\right)\right)$ is under mean CP. Figure 2(b) depicts the mutual correlations between $\sum_{i=1}^{3}a_i\frac{\lambda_i}{k_i}\left(\frac{\boldsymbol{\lambda}}{\mathbf{k}}\right)$, $p\left(\rho_*\left(\frac{\boldsymbol{\lambda}}{\mathbf{k}}\right)\right)$ and $\frac{\boldsymbol{\lambda}}{\mathbf{k}}$. The PP, also known as percolation probability, is the likelihood that a site belongs to an infinite, percolating cluster, signified as $P_\infty\left(\frac{\boldsymbol{\lambda}}{\mathbf{k}}\right)$. In response to the Eq (3.13), we yielded the following findings by

$$P_\infty\left(\frac{\boldsymbol{\lambda}}{\mathbf{k}}\right)=\sum_{i=1}^{3}a_i\frac{\lambda_i}{k_i}-\sum_{i=1}^{3}a_i\frac{\lambda_{*i}}{k_{*i}}\left[\frac{1-\left(a_1\frac{\lambda_1}{k_1}+a_2\frac{\lambda_2}{k_2}+a_3\frac{\lambda_3}{k_3}\right)}{1-\left(a_1\frac{\lambda_{*1}}{k_{*1}}+a_2\frac{\lambda_{*2}}{k_{*2}}+a_3\frac{\lambda_{*3}}{k_{*3}}\right)}\right]^3. \tag{3.14}$$

In addition to strengthening axiom (3.14), we benchmark $\sum_{i=1}^{3}a_i\frac{\lambda_i}{k_i}$ with $\sum_{i=1}^{3}a_i\frac{\lambda_{*i}}{k_{*i}}$, and we inevitably emerge at $P_\infty\left(\frac{\boldsymbol{\lambda}}{\mathbf{k}}\right)\equiv 0$. While $P_\infty\left(\frac{\boldsymbol{\lambda}}{\mathbf{k}}\right)\equiv 0$ rises along with the rebellion of $\theta\left(\frac{\boldsymbol{\lambda}}{\mathbf{k}}\right)$ for $\frac{\boldsymbol{\lambda}}{\mathbf{k}}>\frac{\boldsymbol{\lambda}_c}{\mathbf{k_c}}$, it does not for $\frac{\boldsymbol{\lambda}}{\mathbf{k}}<\frac{\boldsymbol{\lambda}_c}{\mathbf{k_c}}$. The $P_\infty\left(\frac{\boldsymbol{\lambda}}{\mathbf{k}}\right)$ robustness further authenticates $\frac{\boldsymbol{\lambda}}{\mathbf{k}}=\frac{\boldsymbol{\lambda}_c}{\mathbf{k_c}}$ matches to the $\theta\left(\frac{\boldsymbol{\lambda}}{\mathbf{k}}\right)=1$. Also, the

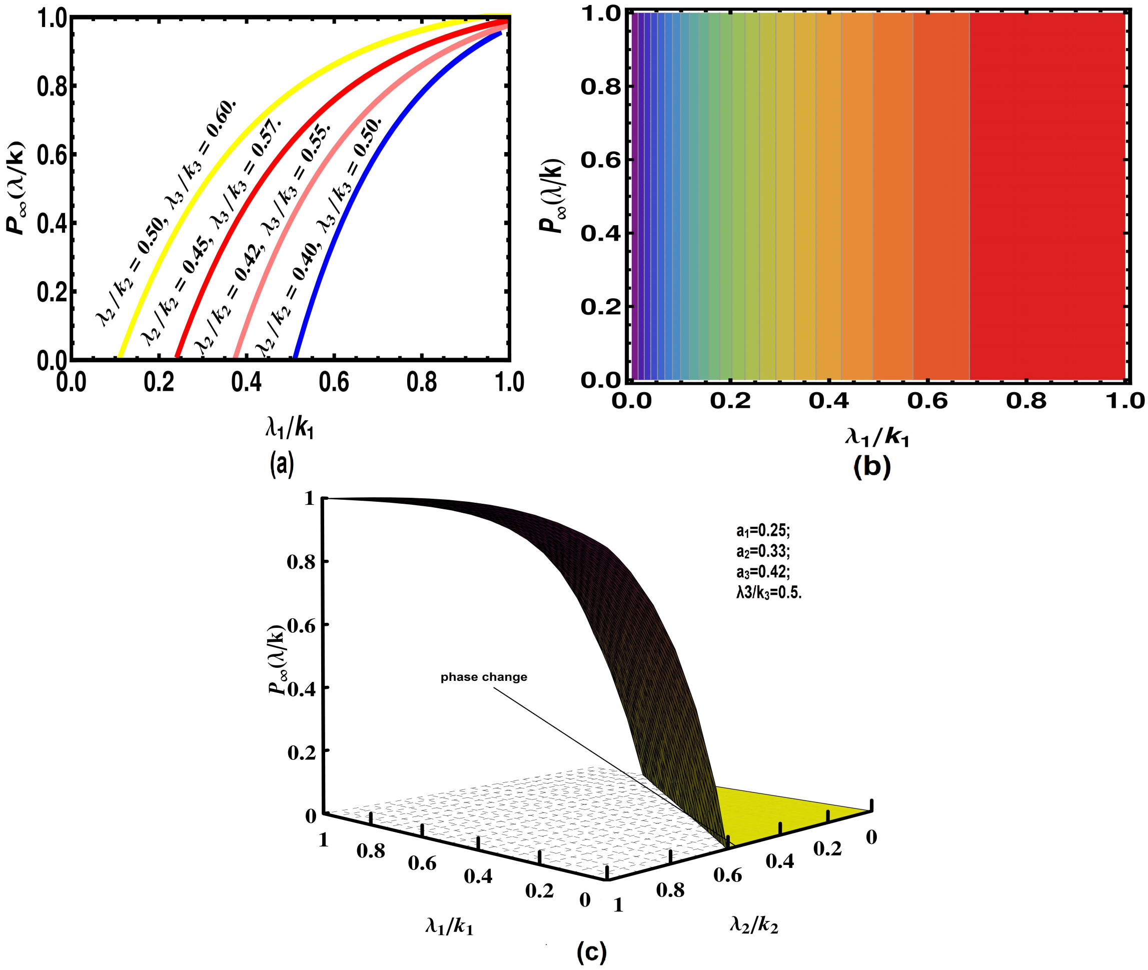

Figure 3. Percolation probability versus CP is figured out for a TNRBL. (**a**) The percolation probability in comparison to $\left(\frac{\lambda_1}{k_1}\right)$, three curves depict the dynamics of percolation probability at different probabilities of $\left(\frac{\lambda_2}{k_2}\right)$ and $\left(\frac{\lambda_3}{k_3}\right)$. (**b**) PP, $P_\infty\left(\frac{\lambda}{\mathbf{k}}\right)$ versus connection probability $\left(\frac{\lambda_1}{k_1}\right)$ at $\left(\frac{\lambda_2}{k_2}\right) = 0.40$ and $\left(\frac{\lambda_3}{k_3}\right) = 0.50$, increases significantly for SCP2. (**c**) PP, $P_\infty\left(\frac{\lambda}{\mathbf{k}}\right)$ versus connection probabilities $\left(\frac{\lambda_1}{k_1}\right)$ and $\left(\frac{\lambda_2}{k_2}\right)$ at $\left(\frac{\lambda_3}{k_3}\right) = 0.4$, for SCP2 optimizes dramatically.

critical surface with CP is the maximum estimate line for $x\left(\frac{\lambda}{\mathbf{k}}\right)$. Even though the critical surface for TNRBL in contexts of CPs only reflects

$$\sum_{i=1}^{3} a_i \frac{\lambda_i}{k_i}(z_i - 2) = 1 \ \text{ for, } \ i = 1,\ 2,\ 3. \tag{3.15}$$

The only thing it is is a line appearing in the plane with connection probability. Thus we can see that $\frac{\lambda}{\mathbf{k}} = \frac{\lambda_c}{\mathbf{k_c}}$, which happens to be suitable for the percolation process, is represented by such symbol $\theta\left(\frac{\lambda}{\mathbf{k}}\right) = 1$. Nonetheless, we employ $\frac{\lambda}{\mathbf{k}} = \frac{\lambda_c}{\mathbf{k_c}}$ to convey it when correctness is required. Conversely, $\sum_{i=1}^{3} a_i \frac{\lambda_i}{k_i}(z_i - 2) < 1$ and $\sum_{i=1}^{3} a_i \frac{\lambda_i}{k_i}(z_i - 2) > 1$ are consistently written as SCP1 and SCP2, correspondingly. As is clear from Eqs (3.14) and (3.15), the algebraic evaluation of our TNRBL features is complex, and determining its limitations is tough. To demonstrate the properties regarding our TNRBL, we employ fixed values with crucial parameters, such as $\mathbf{z} = (3, 4, 5)$ as well as $\boldsymbol{\alpha} = (0.25, 0.33, 0.42)$ in Eqs (3.14) and (3.15), and present the typical percolation, as shown in Figure 2(c).

Three curves illustrating the dynamics that result from PP at various values with the $\left(\frac{\lambda_2}{k_2}\right)$ and $\left(\frac{\lambda_3}{k_3}\right)$ parameters are shown in the Figure 3(a). The Figure 3(b) shows that the numerical value for PP, $P_\infty\left(\frac{\lambda}{\mathbf{k}}\right)$, steadily shift from smaller to higher levels when the values of $\left(\frac{\lambda_1}{k_1}\right)$ increases. The Figure 3(c), demonstrates that the value of PP, $P_\infty\left(\frac{\lambda}{\mathbf{k}}\right)$, progressively shifts from lower to higher as the values of $\left(\frac{\lambda_1}{k_1}\right)$ and $\left(\frac{\lambda_2}{k_2}\right)$. To clarify it from a different perspective, the middle proportion of site distribution accelerates the percolation process. Finally, spanning PP curves shift from right-lower towards left-higher as CPs values change $\left(\frac{\lambda_1}{k_1}\right)$ and $\left(\frac{\lambda_2}{k_2}\right)$. Following the ACS, the mean-field concept-based GRM might be used to show the correctness of the findings. This has the advantage of generating an infinite cluster when the mean number of outgoing nodes exceeds unity. The ACS of finite groups will next be examined.

3.3. Average cluster size of connected sites

Generally, ACS on connected sites is an average size at finite connected sites of clusters (non-percolating). For a cluster of TNRBL with finite size, the probable importance of its size is "l". The probability index of an inevitable occurrence on a site related through l-cluster inclusive of the probability of a site like that connecting via significance finite-cluster is the range of "l" from "0" to ∞, and the probability of it happening is equal. Further explicitly, the probability concerning an event indicating which a site corresponds to a finite cluster is equal to the mean CP for SCP1 and less than the mean CP for SCP2, as shown in (3.13). The probability that an event corresponding to the "l" group (cluster) ought to be separated from the overall probability considering expectation through $P\left(E\left(\frac{\lambda}{\mathbf{k}}\right)\right)$. The ACS of overall finite clusters is procured as a consequence of the specific delineation of expectation appraisal, such as a discrete uncertain variate, for a percolation approach, is provided by

$$
\begin{aligned}
L\left(\frac{\lambda}{\mathbf{k}}\right) &= \sum_{l=1}^{\infty} l \frac{\left\{ l b_l \left(\sum_{i=1}^{3} a_i \frac{\lambda_i}{k_i} \left(1 - \sum_{i=1}^{3} a_i \frac{\lambda_i}{k_i}\right)^{z_i - 3} \right)^l \right\}}{\left(\frac{1}{\left(1 - \sum_{i=1}^{3} a_i \frac{\lambda_i}{k_i}\right)^3} \right) \left\{ \sum_{i=1}^{3} a_i \frac{\lambda_{*i}}{k_{*i}} \left[\frac{1 - \sum_{i=1}^{3} a_i \frac{\lambda_i}{k_i}}{1 - \sum_{i=1}^{3} a_i \frac{\lambda_{*i}}{k_{*i}}} \right]^3 \right\}}, \\
&= \frac{\left[x^2 f'' \left(\sum_{i=1}^{3} a_i \frac{\lambda_i}{k_i} (1 - \overline{p})^{z_i - 3} \right) + x f' \left(\sum_{i=1}^{3} a_i \frac{\lambda_i}{k_i} (1 - \overline{p})^{z_i - 3} \right) \right]}{\left(\frac{1}{\left(1 - \sum_{i=1}^{3} a_i \frac{\lambda_i}{k_i}\right)^3} \right) \left\{ \sum_{i=1}^{3} a_i \frac{\lambda_{*i}}{k_{*i}} \left[\frac{1 - \sum_{i=1}^{3} a_i \frac{\lambda_i}{k_i}}{1 - \sum_{i=1}^{3} a_i \frac{\lambda_{*i}}{k_{*i}}} \right]^3 \right\}}.
\end{aligned}
\tag{3.16}
$$

The precise representation of $L\left(\frac{\lambda}{\mathbf{k}}\right)$ cannot be obtained directly from Eq (3.16) when there is computational complicity. We employed a GRM to obtain the ACS. By starting an addressed sub-branch with a ith type site, we consider D_i, $i = 1, 2, 3$ to indicate a significant contribution to the ACS. Additionally, because identical types of sites occur in the NRBL, the site on behalf of which merely a single sub-bough is in-going, and the remaining are outgoing, there occurs $(z_i - 1)$ sub-divisions which are departing, and every sub-division starts through a jth-sort site in the effective option of a_j, wherever, $j = 1, 2, 3$. Consequently, the involvement of the sub-sub divisions concerning an ith kind site exists $(z_i - 1)(\sum_{i=1}^{3} a_i D_i)$. We get the expression for D_1, D_2, and D_3, respectively.

$$D_1 = \frac{\frac{\lambda_1}{k_1}\left\{1 + a_2\frac{\lambda_2}{k_2}(z_1 - z_2) + a_3\frac{\lambda_3}{k_3}(z_1 - z_3)\right\}}{1 - a_1\frac{\lambda_1}{k_1}(z_1 - 2) - a_2\frac{\lambda_2}{k_2}(z_2 - 2) - a_3\frac{\lambda_3}{k_3}(z_3 - 2)}, \tag{3.17}$$

$$D_2 = \frac{\frac{\lambda_2}{k_2}\left\{1 + a_1\frac{\lambda_1}{k_1}(z_2 - z_1) + a_3\frac{\lambda_3}{k_3}(z_2 - z_3)\right\}}{1 - a_1\frac{\lambda_1}{k_1}(z_1 - 2) - a_2\lambda_2(z_2 - 2) - a_3\frac{\lambda_3}{k_3}(z_3 - 2)}, \tag{3.18}$$

$$D_3 = \frac{\frac{\lambda_3}{k_3}\left\{1 + a_1\frac{\lambda_1}{k_1}(z_3 - z_1) + a_2\frac{\lambda_2}{k_2}(z_3 - z_2)\right\}}{1 - a_1\frac{\lambda_1}{k_1}(z_1 - 2) - a_2\frac{\lambda_2}{k_2}(z_2 - 2) - a_3\frac{\lambda_3}{k_3}(z_3 - 2)}. \tag{3.19}$$

The above formulations assume a particular ith-type site's departing sub-sorts to be z_i when using the above mentioned formulas and assuming that the site in consideration corresponds to the native site. In order to avoid generality cancellation, consider another site to be connected ith-kind site. At that point, it contributes itself together with its z_i, leaving sub-kinds spanning $L\left(\frac{\boldsymbol{\lambda}}{\mathbf{k}}\right)$, $i = 1,\ 2,\ 3$, is given as:

$$\begin{aligned}
L_1\left(\frac{\boldsymbol{\lambda}}{\mathbf{k}}\right) = 1 &+ a_1 z_1\left\{\frac{\frac{\lambda_1}{k_1}\left(1 + a_2\frac{\lambda_2}{k_2}(z_1 - z_2) + a_3\frac{\lambda_3}{k_3}(z_1 - z_3)\right)}{1 - a_1\frac{\lambda_1}{k_1}(z_1 - 2) - a_2\frac{\lambda_2}{k_2}(z_2 - 2) - a_3\frac{\lambda_3}{k_3}(z_3 - 2)}\right\} \\
&+ a_2 z_1\left\{\frac{\frac{\lambda_2}{k_2}\left(1 + a_1\frac{\lambda_1}{k_1}(z_2 - z_1) + a_3\frac{\lambda_3}{k_3}(z_2 - z_3)\right)}{1 - a_1\frac{\lambda_1}{k_1}(z_1 - 2) - a_2\frac{\lambda_2}{k_2}(z_2 - 2) - a_3\frac{\lambda_3}{k_3}(z_3 - 2)}\right\} \\
&+ a_3 z_1\left\{\frac{\frac{\lambda_3}{k_3}\left(1 + a_1\frac{\lambda_1}{k_1}(z_3 - z_1) + a_2\frac{\lambda_2}{k_2}(z_3 - z_2)\right)}{1 - a_1\frac{\lambda_1}{k_1}(z_1 - 2) - a_2\frac{\lambda_2}{k_2}(z_2 - 2) - a_3\frac{\lambda_3}{k_3}(z_3 - 2)}\right\},
\end{aligned} \tag{3.20}$$

$$\begin{aligned}
L_2\left(\frac{\boldsymbol{\lambda}}{\mathbf{k}}\right) = 1 &+ a_1 z_2\left\{\frac{\frac{\lambda_1}{k_1}\left(1 + a_2\frac{\lambda_2}{k_2}(z_1 - z_2) + a_3\frac{\lambda_3}{k_3}(z_1 - z_3)\right)}{1 - a_1\frac{\lambda_1}{k_1}(z_1 - 2) - a_2\frac{\lambda_2}{k_2}(z_2 - 2) - a_3\frac{\lambda_3}{k_3}(z_3 - 2)}\right\} \\
&+ a_2 z_2\left\{\frac{\frac{\lambda_2}{k_2}\left(1 + a_1\frac{\lambda_1}{k_1}(z_2 - z_1) + a_3\frac{\lambda_3}{k_3}(z_2 - z_3)\right)}{1 - a_1\frac{\lambda_1}{k_1}(z_1 - 2) - a_2\frac{\lambda_2}{k_2}(z_2 - 2) - a_3\frac{\lambda_3}{k_3}(z_3 - 2)}\right\} \\
&+ a_3 z_2\left\{\frac{\frac{\lambda_3}{k_3}\left(1 + a_1\frac{\lambda_1}{k_1}(z_3 - z_1) + a_2\frac{\lambda_2}{k_2}(z_3 - z_2)\right)}{1 - a_1\frac{\lambda_1}{k_1}(z_1 - 2) - a_2\frac{\lambda_2}{k_2}(z_2 - 2) - a_3\frac{\lambda_3}{k_3}(z_3 - 2)}\right\},
\end{aligned} \tag{3.21}$$

$$\begin{aligned}
L_3\left(\frac{\boldsymbol{\lambda}}{\mathbf{k}}\right) = 1 &+ a_1 z_3\left\{\frac{\frac{\lambda_1}{k_1}\left(1 + a_2\frac{\lambda_2}{k_2}(z_1 - z_2) + a_3\frac{\lambda_3}{k_3}(z_1 - z_3)\right)}{1 - a_1\frac{\lambda_1}{k_1}(z_1 - 2) - a_2\frac{\lambda_2}{k_2}(z_2 - 2) - a_3\frac{\lambda_3}{k_3}(z_3 - 2)}\right\} \\
&+ a_2 z_3\left\{\frac{\frac{\lambda_2}{k_2}\left(1 + a_1\frac{\lambda_1}{k_1}(z_2 - z_1) + a_3\frac{\lambda_3}{k_3}(z_2 - z_3)\right)}{1 - a_1\frac{\lambda_1}{k_1}(z_1 - 2) - a_2\frac{\lambda_2}{k_2}(z_2 - 2) - a_3\frac{\lambda_3}{k_3}(z_3 - 2)}\right\} \\
&+ a_3 z_3\left\{\frac{\frac{\lambda_3}{k_3}\left(1 + a_1\frac{\lambda_1}{k_1}(z_3 - z_1) + a_2\frac{\lambda_2}{k_2}(z_3 - z_2)\right)}{1 - a_1\frac{\lambda_1}{k_1}(z_1 - 2) - a_2\frac{\lambda_2}{k_2}(z_2 - 2) - a_3\frac{\lambda_3}{k_3}(z_3 - 2)}\right\}.
\end{aligned} \tag{3.22}$$

On average, then, we obtain the ACS for TNRBL via re-collecting the scattering of sites then substituting values of D_1, D_2, and D_3 in the resultant factor, we get the expressions for $L\left(\frac{\boldsymbol{\lambda}}{\mathbf{k}}\right)$, is acquired via

$$L\left(\frac{\boldsymbol{\lambda}}{\mathbf{k}}\right) = 1 + \frac{(a_1z_1 + a_2z_2 + a_3z_3)\left(a_1\frac{\lambda_1}{k_1} + a_2\frac{\lambda_2}{k_2} + a_3\frac{\lambda_3}{k_3}\right)}{1 - \left(a_1\frac{\lambda_1}{k_1}(z_1 - 2) + a_2\frac{\lambda_2}{k_2}(z_2 - 2) + a_3\frac{\lambda_3}{k_3}(z_3 - 2)\right)}, \tag{3.23}$$

above Eq (3.23) shows, the ACS of our proposed method. A mean cluster is Presley more, if $\theta\left(\frac{\lambda}{\mathbf{k}}\right)$ is the enhancing function regarding it. As shown in Eq (3.23), the algebraic comparison of our TNRBL features is complicated, and determining its limiting factor is very difficult.

For the demonstration of the properties of our TNRBL, we employ fixed values spanning critical parameters, such as $\mathbf{z} = (3,\ 4,\ 5)$ and $\boldsymbol{\alpha} = (0.25,\ 0.33,\ 0.42)$ in formulation (3.23), along with typical percolation, illustrated in Figure 4. Referring to the Figure 4(a), an easy-to-find modification of a specific type associated with the phase transition within the CCP line, due to $\theta\left(\frac{\lambda}{\mathbf{k}}\right) = 1$, is presented in the CP regarded as the scheme of percolation. By SCP1, an immeasurable cluster cannot hold themselves acquired; the ACS optimizes with an increment of $\theta\left(\frac{\lambda}{\mathbf{k}}\right)$. In Figure 4(b), we observed that as the connection probability, $\left(\frac{\lambda_3}{k_3}\right) = 0.5$, enlarges, there are more chances to acquire the immeasurable cluster in SCP1, and the ACS enhances at CP with an increment of $\theta\left(\frac{\lambda}{\mathbf{k}}\right)$. In SCP2, an inconceivable cluster might be obtained, and ACS trends towards 0 as connected probabilities also rise. In the subsequent part, we utilized sensitivity analysis to assess the long-term sustainability of the suggested model. Figure 4(c) the ACS, vs the connected probability, $L\left(\frac{\lambda}{\mathbf{k}}\right)$, at $\left(\frac{\lambda_2}{k_2}\right) = 0.45$ and $\left(\frac{\lambda_3}{k_3}\right) = 0.50$. ACS varies from scrutinizing the behavior corresponding to the CCP line during SCP1.

4. Further study regarding the suggested approach

4.1. Sensitivity analysis

The analysis of sensitivity, in a broad sense, is a crucial component of the design of strategies and emphasizes assurance because it stipulates investigations into the validity of the suggested method, the identification that has substantial contributions, the finding of associated relationships between variables that contribute to output and input, and the suggestion of system theory for an individual. We have to utilize a one-factor-at-a-time (OAT) approach based on the characteristics of the suggested method utilized for sensitivity analysis [22, 23, 46, 47]. This technique exists as a simple but effective approach for adjusting OAT to recognize pardon consequences from the output of evoked scheme. Partial derivatives can be employed to calculate sensitivity. The sensitivity index represents the variation ratio in response to variation in the input about constraints or variables. According to recent investigations, we carry out simulation studies on $SI\left(P_\infty, \theta\left(\frac{\lambda}{\mathbf{k}}\right)\right)$ and $SI\left(L, \theta\left(\frac{\lambda}{\mathbf{k}}\right)\right)$, via SI relating response Y to source β.

$$SI(Y,\beta) = \left(\frac{\partial Y}{\partial \beta}\right).\frac{\beta}{Y}, \tag{4.1}$$

the sensitivity index is obtained through Eq (4.1), where Y and β represent the output and input variables, respectively. The SI is denoted by $SI(Y,\beta)$. The right-hand side of Eq (4.1) consists of two components. The first component represents the partial derivative of Y with respect to β, while the

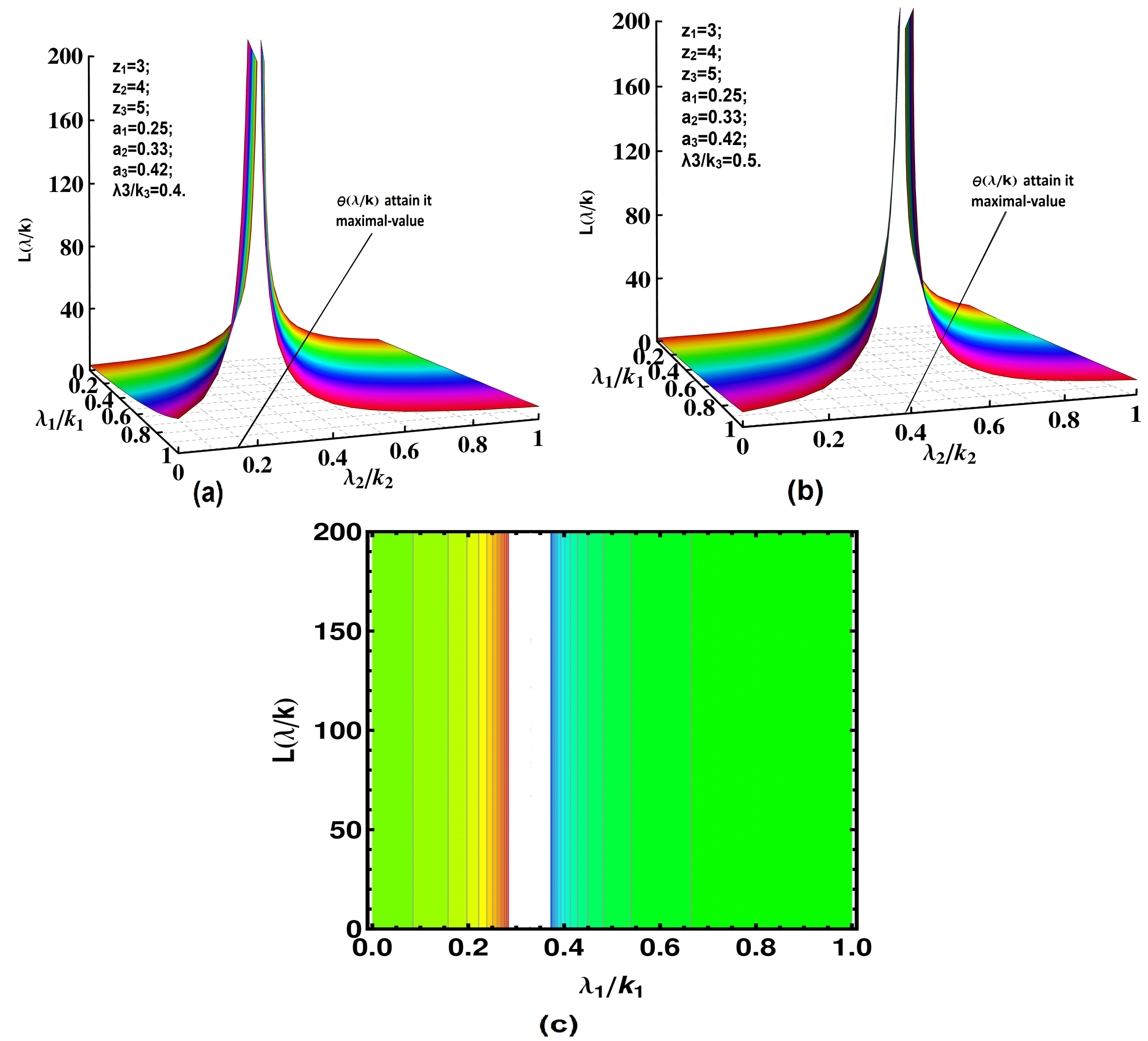

Figure 4. The ACS of the TNRBL with $z_1 = 3$, $z_2 = 4$, and $z_3 = 5$. (**a**), the ACS, $L\left(\frac{\lambda}{\mathbf{k}}\right)$, versus the connected probabilities, $\left(\frac{\lambda_1}{k_1}\right)$ and $\left(\frac{\lambda_2}{k_2}\right)$ at $\left(\frac{\lambda_3}{k_3}\right) = 0.4$. Under SCP1, ACS, $L\left(\frac{\lambda}{\mathbf{k}}\right)$, deviates from seeing the behavior concerning the CCP line (maximal value) $\left(\theta\left(\frac{\lambda}{\mathbf{k}}\right) = 1\right)$. (**b**) $\left(\frac{\lambda_3}{k_3}\right) = 0.5$, regard as the proposed strategy. From (**c**) the ACS, $L\left(\frac{\lambda}{\mathbf{k}}\right)$, versus the connected probability, $\left(\frac{\lambda_1}{k_1}\right)$ at $\left(\frac{\lambda_2}{k_2}\right) = 0.45$ and $\left(\frac{\lambda_3}{k_3}\right) = 0.50$.

second component normalizes the index [22, 23, 47]. The sensitivity index mechanism indicates that a larger absolute value of the index reflects a stronger influence of the input feature on the output response. A negative (positive) sensitivity index denotes an inverse (direct) monotonic relationship between the input and output features within the framework. In this context, $\theta\left(\frac{\lambda}{\mathbf{k}}\right)$ is identified as the dominant sensitivity-related control term, which is closely associated with the connectivity behavior of the TNRBL across SCP1, CP, and SCP2. Therefore, comparing the SI magnitudes of a_i, z_i, and λ_i/k_i helps identify which parameter contributes most strongly to percolation control. The largest SI values near the critical condition provide guidance for targeting the most influential connectivity parameter in intervention design. Currently, we tend to investigate the sensitivity of $\theta\left(\frac{\lambda}{\mathbf{k}}\right)$ to the source parameters, namely (z_1, z_2, z_3) and (a_1, a_2, a_3). As shown, the suggested strategy's constraints are $\sum_{i=1}^{3} a_i = 1$ and $\sum_{i=1}^{3} a_i \frac{\lambda_i}{k_i} = \lambda\left(\frac{\lambda}{\mathbf{k}}\right)$. We designed the SI of $\theta\left(\frac{\lambda}{\mathbf{k}}\right)$ to a_1, a_2, and a_3. Following are the resulting indexes are provided via

$$SI\left(\theta\left(\frac{\boldsymbol{\lambda}}{\mathbf{k}}\right), a_1\right) = \frac{a_1\left\{\left(\frac{\lambda_1}{k_1}\right)(z_1-2) - \left(\frac{\lambda_2}{k_2}\right)(z_2-2) - \left(\frac{\lambda_3}{k_3}\right)(z_3-2)\right\}}{\left\{a_1\left(\frac{\lambda_1}{k_1}\right)(z_1-2) + a_2\left(\frac{\lambda_2}{k_2}\right)(z_2-2) + a_3\left(\frac{\lambda_3}{k_3}\right)(z_3-2)\right\}}, \tag{4.2}$$

$$SI\left(\theta\left(\frac{\boldsymbol{\lambda}}{\mathbf{k}}\right), a_2\right) = \frac{a_2\left\{\left(\frac{\lambda_1}{k_1}\right)(z_1-2) - \left(\frac{\lambda_2}{k_2}\right)(z_2-2) - \left(\frac{\lambda_3}{k_3}\right)(z_3-2)\right\}}{\left\{a_1\left(\frac{\lambda_1}{k_1}\right)(z_1-2) + a_2\left(\frac{\lambda_2}{k_2}\right)(z_2-2) + a_3\left(\frac{\lambda_3}{k_3}\right)(z_3-2)\right\}}, \tag{4.3}$$

$$SI\left(\theta\left(\frac{\boldsymbol{\lambda}}{\mathbf{k}}\right), a_3\right) = \frac{a_3\left\{\left(\frac{\lambda_1}{k_1}\right)(z_1-2) + \left(\frac{\lambda_2}{k_2}\right)(z_2-2) + \left(\frac{\lambda_3}{k_3}\right)(z_3-2)\right\}}{\left\{a_1\left(\frac{\lambda_1}{k_1}\right)(z_1-2) + a_2\left(\frac{\lambda_2}{k_2}\right)(z_2-2) + a_3\left(\frac{\lambda_3}{k_3}\right)(z_3-2)\right\}}. \tag{4.4}$$

Regarding the analogousness of the preceding formulations, we emphasize the SI of $\theta\left(\frac{\lambda}{\mathbf{k}}\right)$ to a_1, which is optimistic and provoking with a_1 for both prerequisites attained by

$$SI\left(\theta\left(\frac{\boldsymbol{\lambda}}{\mathbf{k}}\right), a_1\right) = \begin{cases} \left(\frac{\lambda_1}{k_1}\right)(z_1-2) > \left(\frac{\lambda_2}{k_2}\right)(z_2-2) & \text{optimistic,} \\ \left(\frac{\lambda_1}{k_1}\right)(z_1-2) > \left(\frac{\lambda_3}{k_3}\right)(z_3-2) & \text{optimistic.} \end{cases} \tag{4.5}$$

Therefore, the overall significance of the parameter $SI(\theta\left(\frac{\lambda_1}{k_1}\right), a_1)$ is more substantial because there are larger variations among $\left(\frac{\lambda_1}{k_1}\right)(z_1-2)$, $\left(\frac{\lambda_2}{k_2}\right)(z_2-2)$, and $\left(\frac{\lambda_3}{k_3}\right)(z_3-2)$ is inclined to respond $\theta\left(\frac{\lambda}{\mathbf{k}}\right) = 1$ the distribution regarding probabilities a_i, where, $i = 1, 2, 3$.

We explore the dynamics and complexities of the relationship between output measures $L\left(\frac{\lambda}{\mathbf{k}}\right)$ and $P_\infty\left(\frac{\lambda}{\mathbf{k}}\right)$ with input parameters $L\left(\frac{\lambda}{\mathbf{k}}\right)$ and $P_\infty\left(\frac{\lambda}{\mathbf{k}}\right)$ to $\theta\left(\frac{\lambda}{\mathbf{k}}\right)$, we inquire into the degree of sensitivity $SI\left(P_\infty, \theta\left(\frac{\lambda}{\mathbf{k}}\right)\right)$, which is revealed in Figure 5.

We proceed to the Figure 5(a) It demonstrates that $P_\infty\left(\frac{\lambda}{\mathbf{k}}\right)$, is the enhanced sensitivity contemporary to the critical phase, which is more conveniently, the SI concerning $P_\infty\left(\frac{\lambda}{\mathbf{k}}\right)$ to $\theta\left(\frac{\lambda}{\mathbf{k}}\right)$ corresponds to zero upon SCP1, rapidly scales more closely to the CP, and ultimately tends to decline with the accomplishment of SCP2. The non-negative indices of $SI\left(P_\infty, \theta\left(\frac{\lambda}{\mathbf{k}}\right)\right)$ to $\theta\left(\frac{\lambda}{\mathbf{k}}\right)$ reveal us, $P_\infty\left(\frac{\lambda}{\mathbf{k}}\right)$ enlarges. In addition, we embark on the following Figure 5(b), It illustrates that $P_\infty\left(\frac{\lambda}{\mathbf{k}}\right)$, a boosted sensitivity directly associated with the critical phase, is zero through SCP1, instantly indicators progressively closer to the CP, and subsequently tends to decline with the culmination of SCP2. Consequentially, the Figure 5(c) demonstrates that SI in relation to PP,$SI\left(P_\infty, \theta\left(\frac{\lambda}{\mathbf{k}}\right)\right)$, is even more sensitive at the CP when $\frac{\lambda_3}{k_3} = 0.3$. The mesh's pattern displays its $\left(SI\left(P_\infty, \theta\left(\frac{\lambda}{\mathbf{k}}\right)\right)\right)$ behavior throughout different phases, exhibiting near zero in SCP1 and short-down inclination behavior spanning with accomplishing SCP2.

For further understanding, we present the sensitivity index regarding ACS, $L\left(\frac{\lambda}{\mathbf{k}}\right)$, on 2D and 3D planes, as illustrated in Figure 6. From Figure 6, we observe that $L\left(\frac{\lambda}{\mathbf{k}}\right)$ is more sensitive during the CP $\left(\theta\left(\frac{\lambda}{\mathbf{k}}\right) = 1\right)$, indicating that $SI\left(L, \theta\left(\frac{\lambda}{\mathbf{k}}\right)\right)$ is pessimistic regarding SCP1 and varies based on SCP2. In Figure 6(a), it is evident that the SI acknowledges the increasing complexity of the average size of the cluster, $SI\left(L, \theta\left(\frac{\lambda}{\mathbf{k}}\right)\right)$, at a critical phase, specifically when $\frac{\lambda_3}{k_3} = 0.60$ and $\frac{\lambda_3}{k_3} = 0.70$. The general

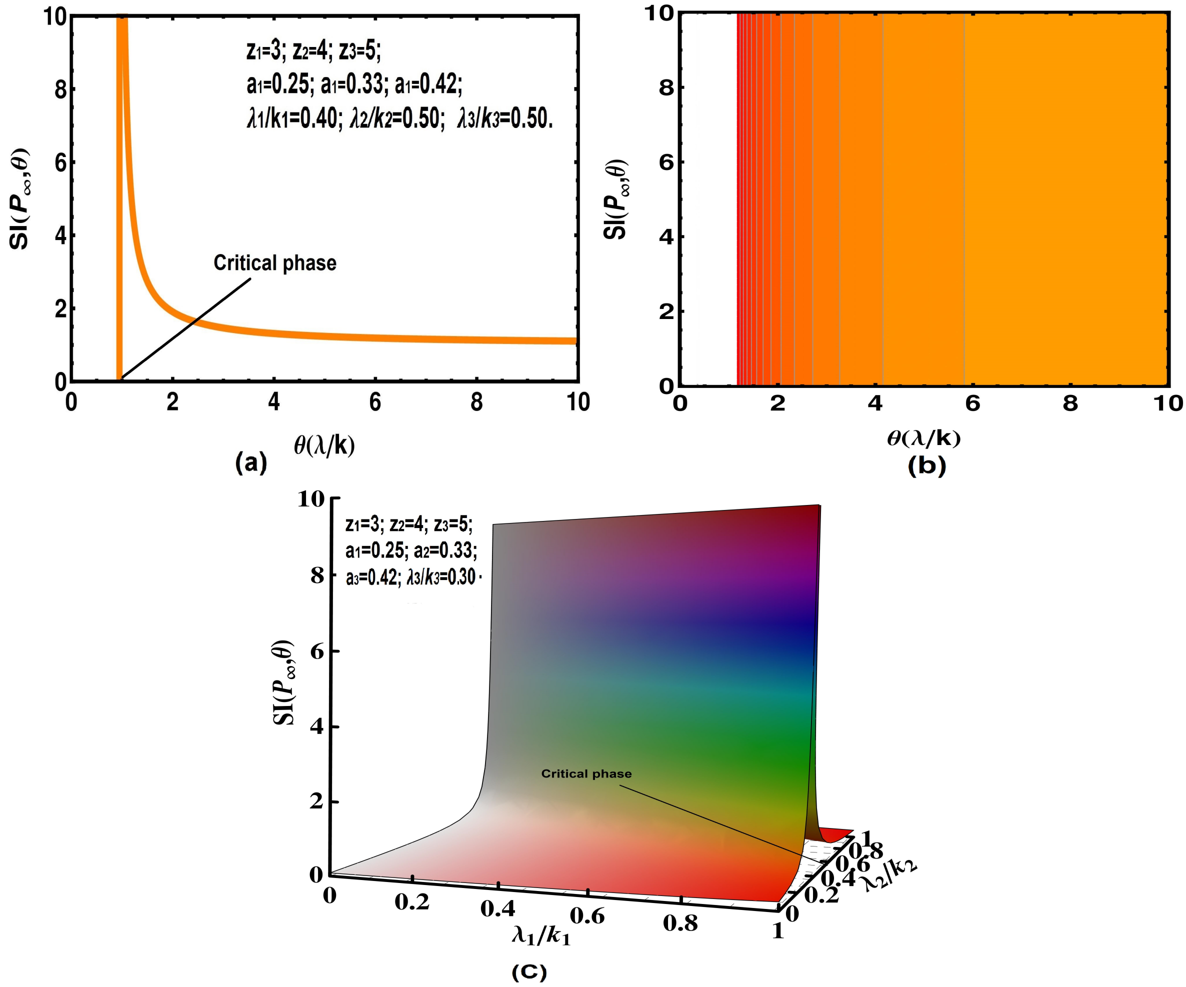

Figure 5. The SI's associated with PP $P_\infty\left(\frac{\lambda}{\mathbf{k}}\right)$ to $\theta\left(\frac{\lambda}{\mathbf{k}}\right)$ for the TNRBL percolation technique $\left\{\frac{\lambda}{\mathbf{k}}; \mathbf{z}, \alpha\right\}$. (**a**) SI pertaining for the PP to $\theta\left(\frac{\lambda}{\mathbf{k}}\right)$, (**b**) SI regarding the PP, $SI\left(P_\infty, \theta\left(\frac{\lambda}{\mathbf{k}}\right)\right)$ in comparison to the connected probability, $\frac{\lambda_1}{k_1}$ at $\frac{\lambda_3}{k_3} = 0.50$ and $\frac{\lambda_3}{k_3} = 0.50$, and (**c**) SI regarding the PP, $SI\left(P_\infty, \theta\left(\frac{\lambda}{\mathbf{k}}\right)\right)$ In comparison to the connected probabilities, $\frac{\lambda_1}{k_1}$ and $\frac{\lambda_2}{k_2}$ at $\frac{\lambda_3}{k_3} = 0.40$.

trend of the mesh shows that $SI\left(L, \theta\left(\frac{\lambda}{\mathbf{k}}\right)\right)$ tends to be positive near SCP1 and negative around SCP2. In Figure 6(a), SI further recognizes that the ACS, $SI\left(L, \theta\left(\frac{\lambda}{\mathbf{k}}\right)\right)$, becomes more intricate at a crucial phase, when $\frac{\lambda_3}{k_3} = 0.60$ and $\frac{\lambda_3}{k_3} = 0.70$. The general pattern of the mesh reflects the $SI\left(L, \theta\left(\frac{\lambda}{\mathbf{k}}\right)\right)$ tendency in different phases, which match the optimistic tendency near SCP1 and the affected area surrounding SCP2. In Figure 6(c), it is again evident that SI recognizes the increasing complexity of the average size of the cluster, $SI\left(L, \theta\left(\frac{\lambda}{\mathbf{k}}\right)\right)$, at a critical phase, specifically when $\frac{\lambda_3}{k_3} = 0.6$. The general trend of the mesh shows that $SI\left(L, \theta\left(\frac{\lambda}{\mathbf{k}}\right)\right)$ tends to be positive near SCP1 and negative around SCP2. The SI determines that $\theta\left(\frac{\lambda}{\mathbf{k}}\right)$ to z_i is $a_i\frac{\lambda_i}{k_i}$, where $i = 1,\ 2,$ and 3. Therefore, we can regulate $\theta\left(\frac{\lambda}{\mathbf{k}}\right)$ more effectively by employing z_i, which corresponds to larger values of $a_i\frac{\lambda_i}{k_i}$, for $i = 1,\ 2,\ 3$. In the previous section, we computed the $SI\left(\theta\left(\frac{\lambda}{\mathbf{k}}\right), a_i\right)$ and $SI\left(\theta\left(\frac{\lambda}{\mathbf{k}}\right), z_i\right)$ and examined the characteristics of these indices. We can now easily analyze how the implications of these variables apply through visual analysis for different

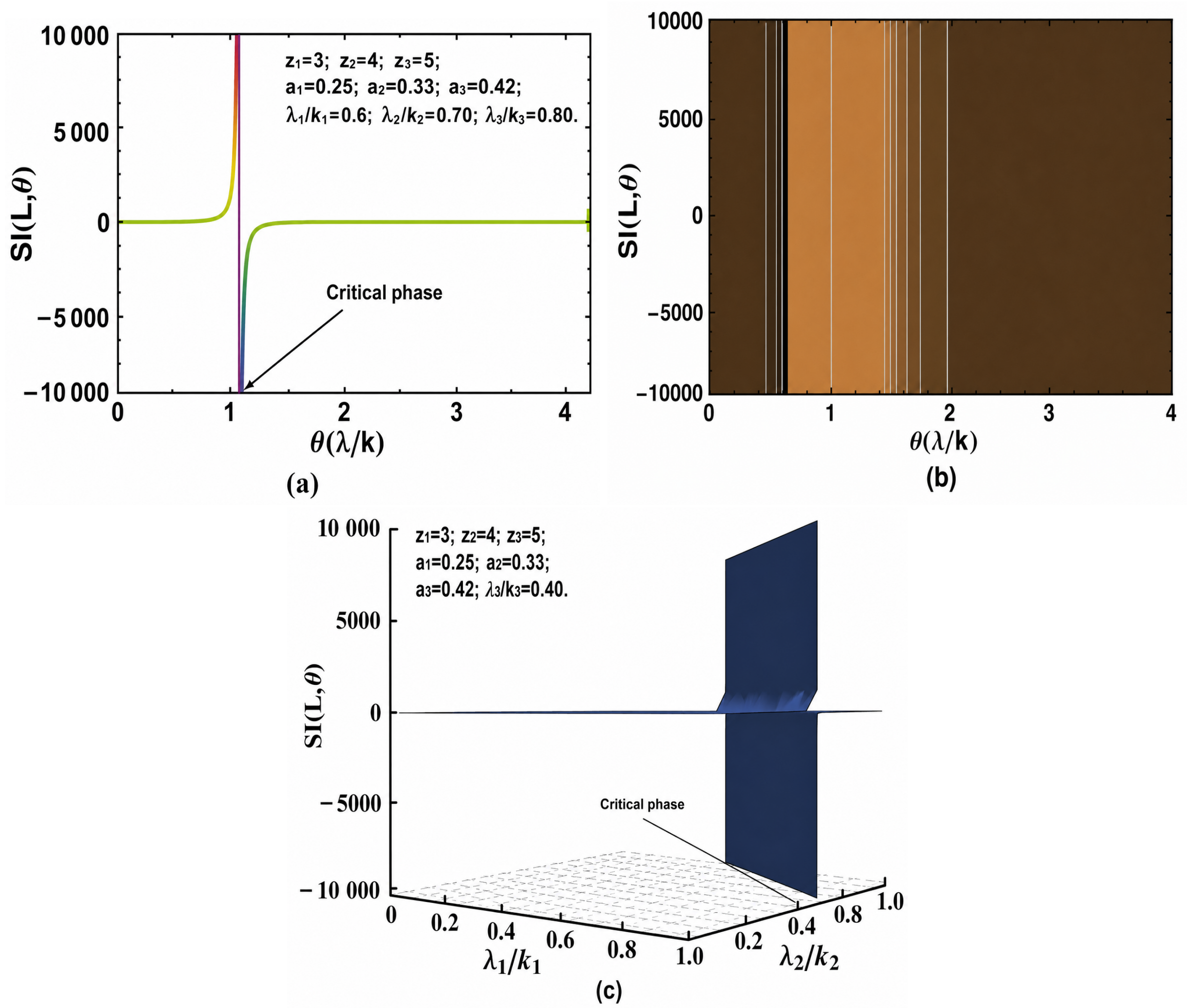

Figure 6. The SI's corresponds to the ACS $L\left(\frac{\lambda}{\mathbf{k}}\right)$ to $\theta\left(\frac{\lambda}{\mathbf{k}}\right)$ for percolation scheme TNRBL $\left\{\frac{\lambda}{\mathbf{k}}; \mathbf{z}, \alpha\right\}$. In (**a**) SI of ACS to $\theta\left(\frac{\lambda}{\mathbf{k}}\right)$, (**b**) SI concerning the ACS of connected sites to $\theta\left(\frac{\lambda}{\mathbf{k}}\right)$, and in the (**c**) SI of ACS to $SI\left(L, \theta\left(\frac{\lambda}{\mathbf{k}}\right)\right)$, versus the connected probabilities, $\frac{\lambda_1}{k_1}$ and $\frac{\lambda_2}{k_2}$ at $\frac{\lambda_3}{k_3} = 0.60$.

indices. By analyzing these findings, we can see that the ACS, $L\left(\frac{\lambda}{\mathbf{k}}\right)$, $P_\infty\left(\frac{\lambda}{\mathbf{k}}\right)$ are pessimistic in SCP1 as well as desirable in SCP2. If we are required to handle the SCP1 framework, we might consider the following scenarios:

$$SI\left(\theta\left(\frac{\boldsymbol{\lambda}}{\mathbf{k}}\right), a_1\right) = \begin{cases} \left(\frac{\lambda_1}{k_1}\right)(z_1 - 2) > \left(\frac{\lambda_2}{k_2}\right)(z_2 - 2) & \text{for } a_1 = 0, \\ \left(\frac{\lambda_1}{k_1}\right)(z_1 - 2) > \left(\frac{\lambda_3}{k_3}\right)(z_3 - 2) & \text{for } a_1 = 0, \\ \left(\frac{\lambda_1}{k_1}\right)(z_1 - 2) < \left(\frac{\lambda_2}{k_2}\right)(z_2 - 2) & \text{for } a_1 = 1, \\ \left(\frac{\lambda_1}{k_1}\right)(z_1 - 2) < \left(\frac{\lambda_3}{k_3}\right)(z_3 - 2) & \text{for } a_1 = 1. \end{cases} \tag{4.6}$$

Alternatively, for $i = 1, 2, 3$, minimize the significance of z_i analogously by adjusting $a_i\left(\frac{\lambda_i}{k_i}\right)$, and then execute the same process for the remaining values. Apart from their theoretical relevance, is our suggested technique also partially relevant to such realistic challenges? To address these conjectures, we also investigate the epidemic diffusion pattern utilizing dynamically altered parameters using the NRBL's non-uniform percolation. We can link connected Bethe lattice sites with infected people and the method for their dispersal by utilizing the following description of the problems associated with the COVID-19 transmission paradigm.

The sensitivity results show that the largest SI magnitudes occur near the critical condition, $\theta\left(\frac{\lambda}{\mathbf{k}}\right) = 1$, where the system becomes highly responsive to small changes in a_i, z_i, and λ_i/k_i. Near this region, minor variations in site distribution, coordination number, or connection probability can strongly affect both the percolation probability $P_\infty\left(\frac{\lambda}{\mathbf{k}}\right)$ and the average cluster size $L\left(\frac{\lambda}{\mathbf{k}}\right)$. The comparative SI behavior indicates that parameters with larger weighted contributions, particularly $a_i\frac{\lambda_i}{k_i}(z_i - 2)$, have the greatest influence on percolation control. Therefore, intervention should mainly target the site type with the highest weighted connectivity contribution by reducing its connection probability λ_i/k_i, limiting its coordination number z_i, or adjusting its distribution probability a_i. In future work, peak SI values for a_i, z_i, and λ_i/k_i will be reported under different lattice configurations to identify the dominant control parameters more precisely and support targeted intervention strategies near the critical connectivity region.

5. Epidemiological application

In Pakistan, as of June 6, 2021, there were an estimated 900,552 infected persons, 817,681 recoveries, and 1,738,484 suspected. Is this the most appropriate COVID-19 infection prevention strategy, and which transmissible diseases utilize this approach? The epidemic spread is, in fact, a percolation process. Percolation has additionally acquired applications in transmitting on lattices (networks), including epidemic methods [48–53]. Through analysis of case-reporting records information spanning May 23, 2020, till June 6, 2021, in Pakistan and government regulation actions, we identify three main epidemic critical phase times: from June 10 to June 27, from November 27 to December 21, and from April 14 to May 12. COVID-19's transmission process is similarly classified into nine stages. Figure 7 illustrates the linkage between percolation parameters, epidemic states (IP, RP, and SP), and phase transitions (SCP1, CP, and SCP2).

Then, using random simulation, we determined that COVID-19 spreads with a significant delay. As a result, we altered the epidemic spreading process's nine phases (S) into: S_1- May 23 until June 9, S_2-June 10 until June 27, S_3-June 28 until July 15, S_4-Nov 1 until Nov 26, S_5-Nov 27 until Dec 21, S_6-Dec 28 until Jun 15, S_7-Mar 16 until Apr 13, S_8-Apr 14 until May 12, and S_9-May 13 until June 6. For further applicability, individuals were classified into three distinct categories based on their physical reversibility, modification, or close association: those at significant risk of infection (infected persons), those who have recovered, and those with a low risk of illness (susceptible individuals). The disease after that appears to be non-uniform percolation upon NRBL 3-connecting and 3-distributing probabilities with their mean contact numbers such as TNRBL $\left\{\left(\frac{\lambda}{k}, \zeta_1\frac{\lambda}{k}, \zeta_2\frac{\lambda}{k}\right); (z_1, z_2, z_3)\left(d_{\frac{\lambda_1}{k_1}}, d_{\frac{\lambda_2}{k_2}}, 1 - d_{\frac{\lambda_1}{k_1}} - d_{\frac{\lambda_2}{k_2}}\right)\right\}$. Here, $\frac{\lambda}{k}$, $\zeta_1\frac{\lambda}{k}$ and $\zeta_2\frac{\lambda}{k}$ are the transmission probabilities concerning an infected person (IP) having a mean contact number (z_1), another recovered person (RP) having a mean contact number (z_2), as well as a susceptible person (SP) having a mean contact number (z_3), $(0 \leq (\zeta_1, \zeta_2) \leq 1)$. The epidemic dissemination modeling employs TNRBL with simulated parameter changes, as shown in the Table 1.

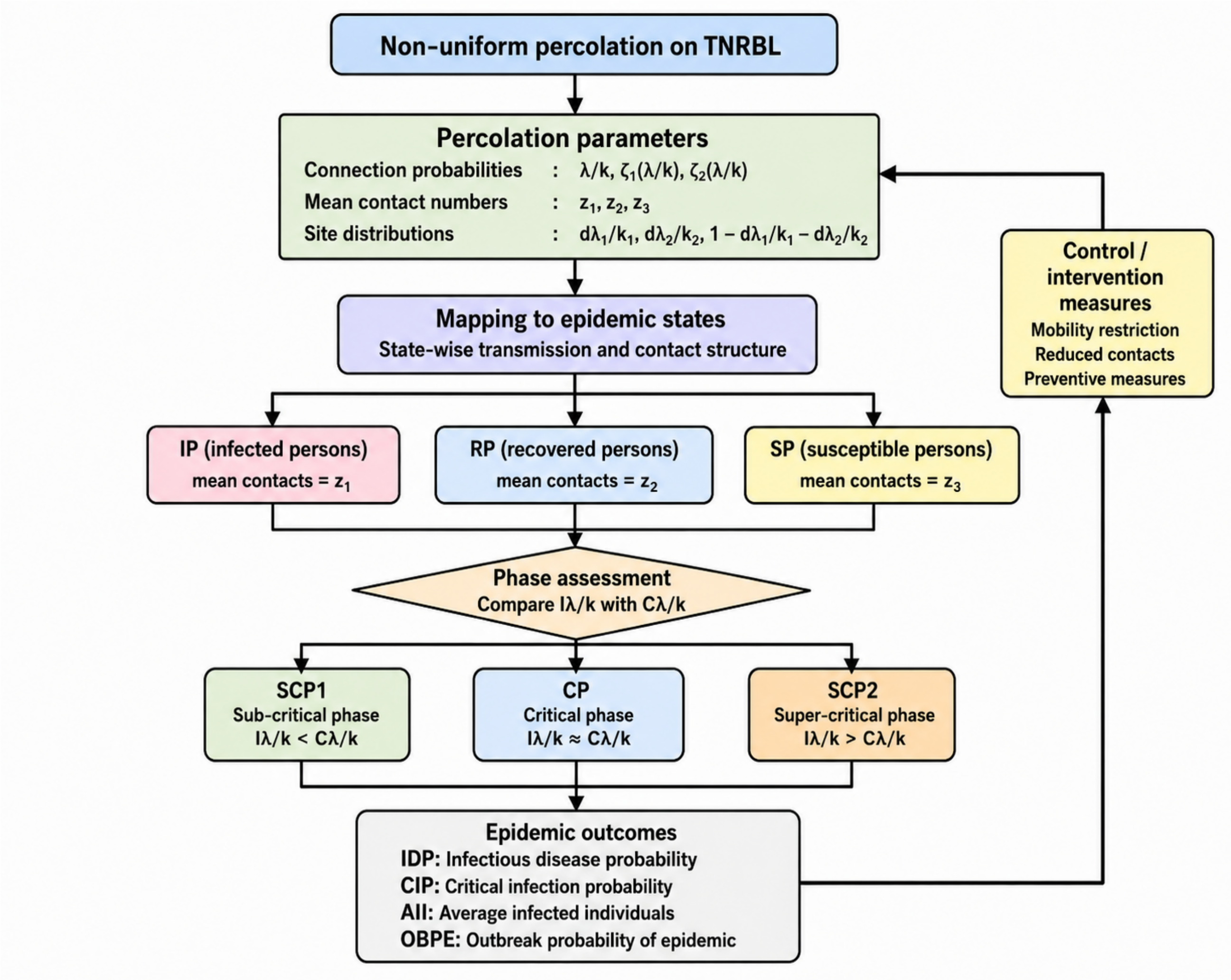

Figure 7. Structural mechanisms for the applicability of non-uniform percolation methodology in epidemic spreading on a non-regular Bethe lattice, linking percolation parameters to epidemic states (IP, RP, and SP) and phase transitions (SCP1, CP, and SCP2).

From Table 1, various aspects must be considered, including $I_{\frac{\lambda}{k}}$, $D_{\frac{\lambda}{k}}$, $C_{\frac{\lambda_c}{\mathbf{k}_c}}$, $A\left(\frac{\lambda}{\mathbf{k}}\right)$, and $P_\infty\left(\frac{\lambda}{\mathbf{k}}\right)$, which represent the IDP (Infectious Disease Probability), the probability of critical infection (CIP), the average infected individual (AII), and the outbreak probability epidemic (OBPE), respectively. We performed a Monte Carlo simulation to evaluate the dependent relationships between $I_{\frac{\lambda}{k}}$, $C_{\frac{\lambda_c}{\mathbf{k}_c}}$, and the infected individuals, using illusive parameters to develop more accurate and meticulous disease-control strategies.

The epidemic data dispersion shows the mean number concerning contacts for a single infected, single recovered, and a single suspected individual, as well as the infection probability in FW (S_1, S_2, and S_3). Following the statistical investigation's subject demographic, we chose the following values: $\zeta_1 = 0.45$ and $\zeta_1 = 0.55$, are used in the epidemic modeling. Individuals must grasp that the virus's degree of spread, though only slightly increased by the preventative method, represents infection probabilities during various phases. Consequently, the probability of infection spreading to the SW has shifted. Other factors might change as an effect of inhibition, whereas restriction parameters stay constant between stages (S_4, S_5 and S_6). The total number of associations among an infected person, recovered person, and suspected person, as well as their corresponding infected likelihood, as well as the restriction parameters, remain unaltered for the reason of evaluating the statistical significance of TW (S_7, S_8 and S_9). It is vital to highlight that infection possibilities are minimal at different stages of TW and are unaffected by prudent decisions. The epidemic spreading paradigm (in Pakistan) is vital in developing the suggested framework. Table 1 provides information about the division methodology in addition to parameters. In S_1 during epidemic's FW, along with the above analysis, $z_1 = 4$, $z_2 = 14$, $z_3 = 4$, $\frac{\lambda}{\mathbf{k}} = 0.3101$, and $\frac{\lambda_c}{\mathbf{k}_c} = 0.3497$, according with the parameters above, $I_{\frac{\lambda}{k}}$ every day is simulated.

Table 1. Simulated and statistical analysis of the TNRBL in relation to COVID-19 parameters.

Data	Groups	$I_{\lambda/\mathbf{k}}$	ACN ($\mathbf{z}$)	PDP ($D_{\lambda/\mathbf{k}}$)	CIP ($C_{\lambda_c/\mathbf{k}_c}$)	AII $A(\lambda/\mathbf{k})$	OBPE ($P_\infty(\lambda/\mathbf{k})$)
	S_1	0.3101	(4,14,4)	(0.18,0.64,0.17)	22.85	6.463	0.036
FW	S_2	0.3778	(6,9,4)	(0.32,0.47,0.11)	24.41	9.016	0.081
	S_3	0.3778	(7,8,3)	(0.38,0.45,0.16)	9.945	7.808	0.040
	S_4	0.1042	(16,13,11)	(0.40,0.32,0.27)	2.345	1.054	zero
SW	S_5	0.2696	(15,14,9)	(0.40,0.37,0.41)	12.69	3.116	0.001
	S_6	0.3774	(17,12,8)	(0.47,0.32,0.21)	11.42	2.523	zero
	S_7	0.3774	(10,18,6)	(0.29,0.52,0.17)	34.08	2.026	zero
TW	S_8	0.3030	(12,13,5)	(0.40,0.43,0.18)	45.08	3.454	0.007
	S_9	0.3030	(18,12,7)	(0.48,0.22,0.19)	6.602	1.426	zero

Overall epidemic data analysis via our TNRBL model, as shown by Figure 8, indicates that it is significantly feasible for such real-life scenarios. From Figure 8(a), the number of infected people shows an increasing trend, implying that the disease affects a large population. Until recently, in S_2, some preventive measures needed necessary to prevent the perception regarding the circumstance, thus parameters are changed to $z_1 = 6$, $z_2 = 9$, $z_3 = 4$, $\frac{\lambda}{\mathbf{k}} = 0.3778$, and $\frac{\lambda_c}{\mathbf{k}_c} = 0.3778$, as in Figure 8(b). In S_3, the seriousness of epidemic is continually being determined, and extra security precautions are procured. At the same time, parameters decline in besides $z_1 = 7$, $z_2 = 8$, $z_3 = 3$, $\frac{\lambda}{\mathbf{k}} = 0.3778$, and $\frac{\lambda_c}{\mathbf{k}_c} = 0.2862$.

The findings in this stage reveal that vary with the downward tendency providing would occur when it reached zero immediately after a set period, which conditions the influence of transmittable illness, can be managed without any further measures, as shown in the Figure 8(c). We also corresponded about the COVID-19 SW findings. From the following Figure 8(d), Its gradual steepness of $I_{\frac{\lambda}{k}}$ indicates epidemic transmission. In S_4, safeguards are required along with an identification of the condition; therefore parameters changed to $z_1 = 16$, $z_2 = 13$, $z_3 = 11$, $\frac{\lambda}{\mathbf{k}} = 0.1042$, and $\frac{\lambda_c}{\mathbf{k}_c} = 0.4595$. We found that $I_{\frac{\lambda}{k}}$ varies chaotically when investigating S_5, as seen in the Figure 8(e). Constantly, in S_5, the severity of the pandemic gradually became identified. So, in S_5 we can further safeguard measures were acquired, and limitations decreased further to $z_1 = 5$, $z_2 = 14$, $z_3 = 9$, $\frac{\lambda}{\mathbf{k}} = 0.2696$, and $\frac{\lambda_c}{\mathbf{k}_c} = 0.2696$. The S_6, as demonstrates that on $I_{\frac{\lambda}{k}}$, which establishes the influence of COVID-19, fluctuates with the decay drift progressively over a period and might be limited in the absence of partially further measurements

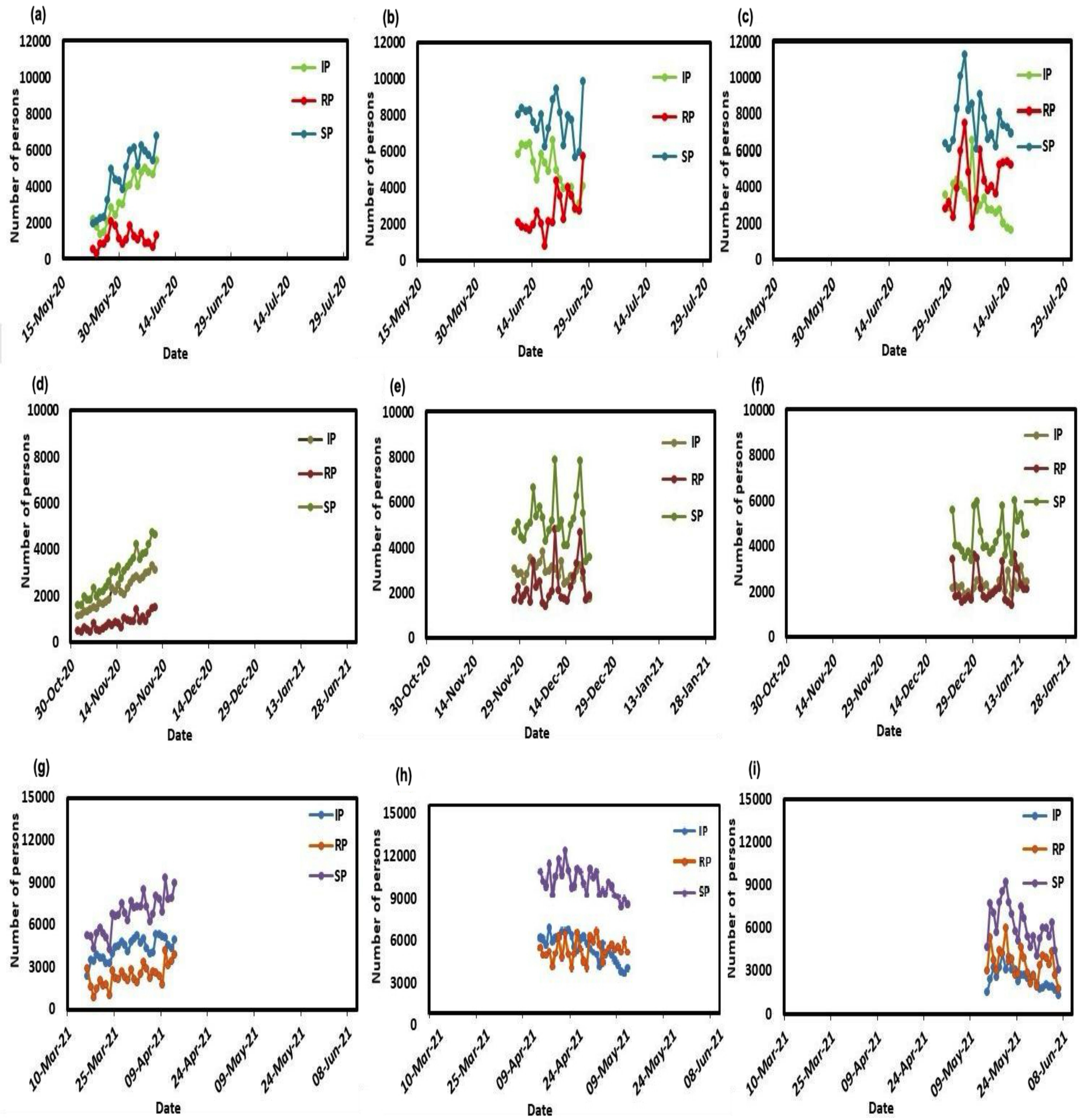

Figure 8. The number of infected, recovered, and suspected individuals over time is analyzed based on the probabilities of $I_{\frac{\lambda}{k}}$ being less than, equal to, or greater than $C_{\frac{\lambda}{k}}$. These probabilities, represented as IP, RP, and SP, correspond to the infected, recovered, and suspected categories in the COVID-19 datasets (FW, SW, and TW).

with such parameters, $z_1 = 17$, $z_2 = 12$, $z_3 = 8$, $\frac{\boldsymbol{\lambda}}{\mathbf{k}} = 0.3774$, and $\frac{\boldsymbol{\lambda_c}}{\mathbf{k}_c} = 0.3640$, as shown in the above Figure 8(f).

Figure 8(g) demonstrates that the TW of COVID-19 indicates the propagation of the pandemic with a more incremental $I_{\frac{\lambda}{k}}$ upward gradient. Precautionary precautions were necessary for S_7 due to the intensity of the pandemic. Therefore, the parameters be modified to $z_1 = 10$, $z_2 = 18$, $z_3 = 6$,

$\frac{\lambda}{\mathbf{k}}$ = 0.3774, and $\frac{\lambda_c}{\mathbf{k}_c}$ = 0.3612. From Figure 8(h), via meticulously examination of S_8, we discovered that $I_{\frac{\lambda}{k}}$ fluctuates randomly in terms of occurrence. Therefore, alertness completes the epidemic by identifying the era with extra protective measures by adjusting the restrictions to $z_1 = 12$, $z_2 = 13$, $z_3 = 5$, $\frac{\lambda}{\mathbf{k}}$ = 0.3030, and $\frac{\lambda_c}{\mathbf{k}_c}$ = 0.3030. The $I_{\frac{\lambda}{k}}$ variable diverges in the subsequent inquiry, S_9, with a period-by-period small decline drift; it is the visible epidemic spread. Considering these constraints $z_1 = 18, z_2 = 12, z_3 = 7$, $\frac{\lambda}{\mathbf{k}}$ = 0.3030, and $\frac{\lambda_c}{\mathbf{k}_c}$ = 0.3953, as seen in the Figure 8(i). In the overall epidemic transmitting's waves pattern, S_1, S_4 and S_7 are in SCP1, S_2, S_5 and S_8, while S_3, S_6 and S_9 are in SCP2. Therefore, a significant modification in epidemic inclination would result from reaching the CP and marginally altering the design parameters. Thus, in large-scale illness outbreaks, we limit in SCP1 provided the $I_{\frac{\lambda}{k}}$ is merely smaller than the $C_{\frac{\lambda}{k}}$. The probability of an extensive epidemic breakout in the situation of SCPI is minimal. If $I_{\frac{\lambda}{k}}$ reaches and crosses $C_{\frac{\lambda}{k}}$, the probability increases by a power law with exponent one according to their differences, then the syndrome swiftly spread. Therefore, we prefer to reduce outside movements, using the general public as a practical approach for the incubation period of the infectious condition. It significantly hampers the social life of communities, in any case.

COVID-19 case study is presented as an application-based demonstration of the proposed TNRBL framework rather than as a conventional day-wise forecasting model. In this framework, z_1, z_2, z_3 represent the mean contact numbers of the infected, recovered, and susceptible groups, respectively, while ζ_1 and ζ_2 are transmission-scaling parameters used to reflect stage-wise changes in transmission intensity. The TNRBL model provides a structural percolation-based interpretation of epidemic connectivity by incorporating non-uniform contact patterns, heterogeneous population states, and variation in connection probability. However, detailed forecasting-level validation is left for future work. Future studies will fit the simulated daily infection trends to observed epidemic data using RMSE, MAE, and R^2, and will compare the predictive performance of the TNRBL framework with conventional SIR and SEIR models.

6. Conclusions

The current work proposed a novel dynamic percolation strategy, in which a higher fraction of connections and distribution probabilities enhances the significance of the NRBL model. This approach is applied to explore the transmission challenges associated with COVID-19. In summary, non-uniform dynamical percolation is significant for our NRBL, demonstrating key percolation characteristics and exhibiting cluster properties. This investigation obtained precise calculations for percolation quantities (CSD, CCP, PP, and ACS). Sensitivity analysis provides quantitative measures that can inform effective control strategies in complex scenarios. The critical percolation scenario highlights sensitive points where small changes cause significant phase shifts, providing valuable insights for early detection at SCP1. This phase remains the most sensitive to changes in the system's behavior, limiting the robustness of the method during transitions. We observed that ACS and PP are favorable in SCP1 and desirable in SCP2, but exhibit higher sensitivity at the CP. By linking connected Bethe lattice sites with infected, recovered, and suspected individuals, we provide a framework to address the complexities of COVID-19 transmission. Thus, non-uniform percolation on NRBL presents a robust approach to understanding the dynamic diffusion behavior of COVID-19. Several other problems remain for further investigation, including non-uniform percolation on lattices with alternative random mechanisms such as andom graphs on more complex networks.

Data availability statements

The following data was supplied concerning statistics' availability. We used the information for daily confirmed cases of COVID-19. The WHO and the National Institute for Health (NIH) in Islamabad, Pakistan, provided the time frame, which spanned from May 23, 2020, through June 6, 2021.(i) https://covid.gov.pk/; (ii) https://www.who.int/.

Use of AI tools declaration

The author declare he has not used Artificial Intelligence (AI) tools in the creation of this article.

Acknowledgments

The author would like to express his sincere gratitude to Professor Jingli Ren for his valuable guidance, insightful suggestions, and continuous support throughout this research.

Conflict of interest

The author declare that he has no competing interests.

References

1. Rücker M, Berg S, Armstrong RT, Georgiadis A, Ott H, Schwing A, et al. (2015) From connected pathway flow to ganglion dynamics. *Geophys Res Lett* 42: 3888–3894. https://doi.org/10.1002/2015GL064007

2. Brentjes S, (2020) Wilbur R. Knorr on Thābit ibn Qurra: A case-study in the gistoriography of premodern science. *Aestimatio* 1: 113–172. https://doi.org/10.33137/aestimatio.v1i1.37604

3. Estrada E, (2010) Quantifying network heterogeneity, *Phys Rev E Stat Nonlinear Soft Matter Phys* 82: 066102. https://doi.org/10.1103/PhysRevE.82.066102

4. Lawler G, Schramm O, Werner W, (2022) One-arm exponent for critical 2D percolation. *Electron J Probab* 7: 1–13. https://doi.org/10.1214/EJP.v7-101

5. Schramm O, A percolation formula. *Electron J Probab* 6: 115–120. https://doi.org/10.1214/ECP.v6-1041

6. Grimmett G, (1999) What is percolation?, In: *Percolation*, Springer, 1–31. https://doi.org/10.1007/978-3-662-03981-6_1

7. Grimmett GR, Manolescu I, (2013) Inhomogeneous bond percolation on square, triangular and hexagonal lattices. *Ann Probab* 41: 2990–3025. https://doi.org/10.1214/11-AOP729

8. Kesten H, (1982) *Percolation Theory for Mathematicians*, Boston: Birkhäuser. https://doi.org/10.1007/978-1-4899-2730-9

9. Turban LC, (1979) Anisotropic percolation on the Bethe lattice. *J Phys C Solid State Phys* 12: 1479–1490. https://doi.org/10.1088/0022-3719/12/8/010

10. Deng Y, Ouyang Y, Blöte HWJ, (2019) Medium-range percolation in two dimensions. *J. Phys Conf Ser* 1163: 012001. https://doi.org/10.1088/1742-6596/1163/1/012001

11. Malik O, Varga M, Moussawi A, Hunt D, Szymanski BK, Toroczkai Z, et al. (2022) Diffusive persistence on disordered lattices and random networks. *Phys Rev E* 109: 024113. https://doi.org/10.1103/PhysRevE.109.024113

12. Ouyang Y, Deng Y, Blöte HWJ, (2018) Equivalent-neighbor percolation models in two dimensions: Crossover between mean-field and short-range behavior. *Phys Rev E* 98: 062101. https://doi.org/10.1103/PhysRevE.98.062101

13. Ren J, Zhang L, Siegmund S, (2016) How inhomogeneous site percolation works on Bethe lattices: Theory and application. *Sci Rep* 6: 1–11. https://doi.org/10.1038/srep22420

14. Xun Z, Hao D, Ziff RM, (2021) Site percolation on square and simple cubic lattices with extended neighborhoods and their continuum limit. *Phys Rev E* 103: 022126. https://doi.org/10.1103/PhysRevE.103.022126

15. Ziff RM, Scullard CR, Wierman JC, Sedlock MR, (2012) The critical manifolds of inhomogeneous bond percolation on bow-tie and checkerboard lattices. *J Phys A Math Theor* 45: 494005. https://doi.org/10.1088/1751-8113/45/49/494005

16. Zhang L, Ren J, (2019) Inhomogeneous percolation on multilayer networks. *J Stat Mech Theory Exp* 2019: 033204. https://doi.org/10.1088/1742-5468/ab02ea

17. Angst S, Wolf DE, (2016) Network theory for inhomogeneous thermoelectrics. *New J Phys* 18: 043004. https://doi.org/10.1088/1367-2630/18/4/043004

18. Bighin G, Enss T, Defenu N, (2022) Universal scaling in real dimension. preprint, arXiv:2211.13302. https://doi.org/10.48550/arXiv.2211.13302

19. Bradly CJ, Owczarek AL, (2021) Effect of lattice inhomogeneity on collapsed phases of semi-stiff ISAW polymers. *J Stat Phys* 182: 1–12. https://doi.org/10.1007/s10955-021-02701-9

20. Li X, Nakagawa S, Tsuji Y, Watanabe N, Shibayama M, (2019) Polymer gel with a flexible and highly ordered three-dimensional network synthesized via bond percolation. *Sci Adv* 5: eaax8647. https://doi.org/10.1126/sciadv.aax8647

21. Ren J, Zhang L, (2017) Inhomogeneous site percolation on an irregular bethe lattice with random site distribution. *J Stat Phys* 168: 394–407. https://doi.org/10.1007/s10955-017-1803-1

22. Shahid MI, Chen C, Ren J, (2023) Inhomogeneous percolation on the Bethe lattice with critical exponents and its application. *Results Phys* 51: 106631. https://doi.org/10.1016/j.rinp.2023.106631

23. Shahid MI, Xiong NN, Ren J, (2023) A novel method for the 3D inhomogeneous percolation on the lattice with its application. *Results Phys* 46: 106275. https://doi.org/10.1016/j.rinp.2023.106275

24. Villegas P, Gili T, Gabrielli A, Caldarelli G, (2022) Characterizing spatia point processes by percolation transitions. *J Stat Mech Theory Exp* 2022: 073202. https://doi.org/10.1088/1742-5468/ac7a2c

25. Zhang B, Gao H, Xiao C, Tong X, Chen Y, (2020) The trade-off between membrane permselectivity and conductivity: A percolation simulation of mass transport. *J Membr Sci* 597: 117751. https://doi.org/10.1016/j.memsci.2019.117751

26. Magare S, Roy AK, Srivastava V, (2022) 1D Ising model using the Kronecker sum and Kronecker product. *Eur J Phys* 43: 035102. https://doi.org/10.1088/1361-6404/ac5637

27. Nie Y, Zhong X, Lin T, Wang W, (2023) Pathogen diversity in meta-population networks. *Chaos Solitons Fractals* 166: 112909. https://doi.org/10.1016/j.chaos.2022.112909

28. Roden CA, Dai Y, Giannetti CA, Seim I, Lee M, Sealfon R, et al. (2022) Double-stranded RNA drives SARS-CoV-2 nucleocapsid protein to undergo phase separation at specific temperatures. *Nucleic Acids Res* 50: 8168–8192. https://doi.org/10.1093/nar/gkac596

29. Herrera DR, Ramírez JE, Velázquez-Castro J, Díaz B, Martínez MI, Juárez PV, et al. (2021) Mobility strategies based on percolation theory to avoid the spread of diseases: COVID-19. preprint, arXiv:2105.10934. https://doi.org/10.48550/arXiv.2105.10934

30. Zhang L, (2022) *A New Triggering Mechanism of the Boiling Crisis Based on the Percolation Theory and Its Implication*, Ph.D thesis, Massachusetts Institute of Technology.

31. Bzai JSA, (2023) *Enhancing Performance of Big Data Applying Similarity Over Detected Community*, Ph.D thesis, University of Belgrade (Serbia).

32. Ciacci A, (2022) *Stories from Different Worlds in the Universe of Complex Systems*, Ph.D thesis, Imperial College London.

33. Garrod M, (2020) *Influence and Ensemble Variability in Unobserved Networks*, Ph.D thesis, Imperial College London.

34. Maruyama M, (2022) Urban governance of the COVID-19 pandemic in Japan: An urban political sociological approach to the case of Osaka. *Jpn J Sociol* 31: 7–22. https://doi.org/10.1111/ijjs.12135

35. Hernández-Lemus E,(2021) Random fields in physics, biology and data science. *Front Phys* 9: 641859. https://doi.org/10.3389/fphy.2021.641859

36. Hurd TR, (2021) COVID-19: Analytics of contagion on inhomogeneous random social networks. *Infect Dis Modell* 6: 75–90. https://doi.org/10.1016/j.idm.2020.11.001

37. Surano FV, (2023) *Unveiling Human Interactions: Approaches and Techniques Toward the Discovery and Representation of Interactions in Networks*, Ph.D thesis, Politecnico di Torino.

38. Wang XJ, Hu H, Huang C, Kennedy H, Li CT, Logothetis N, et al. (2020) Computational neuroscience: A frontier of the 21st century. *Natl Sci Rev* 7: 1418–1422. https://doi.org/10.1093/nsr/nwaa129

39. Xiong X, Zeng Z, Feng M, Szolnoki A, (2024) Coevolution of relationship and interaction in cooperative dynamical multiplex networks. *Chaos* 34: 023118. https://doi.org/10.1063/5.0188168

40. Zhao X, Wu C, Chen CC, Zhou Z, (2022) The influence of corporate social responsibility on incumbent employees: A meta-analytic investigation of the mediating and moderating mechanisms. *J Manage* 48: 114–146. https://doi.org/10.1177/0149206320946108

41. Eleftheriadis E, (2024) *The Cure for World Peace: A Public Health Strategy*, Bachelor's honors thesis, University of San Diego. https://doi.org/10.22371/02.2024.008

42. The South African Technology Network (SATN) in partnership with National Scientists and Organisations, Priority Setting for Intervenfions in Pre and Post Pandemic Management: The Case of COVID-19, 2020. Available from: https://thensa.co.za/wp-content/uploads/2020/09/SATN-COVID-19-Position-Paper-030620-20200921.pdf.

43. Singal AG, Yarchoan M, Yopp A, Sapisochin G, Pinato DJ, Pillai A, (2024) Neoadjuvant and adjuvant systemic therapy in HCC: Current status and the future. *Hepatol Commun* 8: e0430. https://doi.org/10.1097/HC9.0000000000000430

44. Novotny TE, (2022) Ethics and public health 11, In: *Issues in Public Health: Challenges for the 21st Century*, McGraw-Hill Education, 227.

45. Olumegbon B, (2023) *A Case Study of the Political Determinant of Health on the Public Health Crisis of Malaria in Nigeria*, Ph.D thesis, Abilene Christian University.

46. Puszyński K, Lachor P, Kardyńska M, Śmieja J, (2012) Sensitivity analysis of deterministic signaling pathways models. *Bull Pol Acad Sci Tech Sci* 60: 471–479. https://doi.org/10.2478/v10175-012-0060-3

47. Saltelli A, Ratto M, Andres T, Campolongo F, Cariboni J, Gatelli D, et al. (2008) *Global Sensitivity Analysis: The Primer*, John Wiley & Sons. https://doi.org/10.1002/9780470725184

48. Altmann DM, Boyton RJ, (2022) COVID-19 vaccination: The road ahead. *Science* 375: 1127–1132. https://doi.org/10.1126/science.abn1755

49. Croccolo F, Roman HE, (2020) Spreading of infections on random graphs: A percolation-type model for COVID-19. *Chaos Solitons Fractals* 139: 110077. https://doi.org/10.1016/j.chaos.2020.110077

50. Danon L, Lacasa L, Brooks-Pollock E, (2021) Household bubbles and COVID-19 transmission: Insights from percolation theory. *Philos Trans R Soc B* 376: 20200284. https://doi.org/10.1098/rstb.2020.0284

51. Deng H, Du J, Gao J, Wang Q, (2021) Network percolation reveals adaptive bridges of the mobility network response to COVID-19. *PloS One*, 16: e0258868. https://doi.org/10.1371/journal.pone.0258868

52. Franco C, Ferreira LS, Sudbrack V, Borges ME, Poloni S, Prado PI, et al. (2022) Percolation across households in mechanistic models of non-pharmaceutical interventions in SARS-CoV-2 disease dynamics. *Epidemics* 39: 100551. https://doi.org/10.1016/j.epidem.2022.100551

53. Galeazzi A, Cinelli M, Bonaccorsi G, Pierri F, Schmidt AL, Scala A, et al. (2021) Human mobility in response to COVID-19 in France, Italy and UK. *Sci Rep* 11: 1–10. https://doi.org/10.1038/s41598-021-92399-2

54. Broadbent SR, Hammersley JM, (1957) Percolation processes: I. Crystals and mazes. In: *Mathematical Proceedings of the Cambridge Philosophical Society*, Cambridge University Press, 629–641. https://doi.org/10.1017/S0305004100032680

55. Burlak G, Calderón-Segura Y, (2014) Percolation and lasing in real 3D crystals with inhomogeneous distributed random pores. *Phys B Condens Matter* 453: 8–13. https://doi.org/10.1016/j.physb.2014.04.030

56. Barequet G, Shalah M, (2022) Improved upper bounds on the growth constants of polyominoes and polycubes. *Algorithmica*, 84: 3559–3586. https://doi.org/10.1007/s00453-022-00948-6

57. Bergmann S, Kissel S, Külske C, (2023) Dynamical Gibbs-non-Gibbs transitions in Widom-Rowlinson models on trees. In: *Annales De L'Institut Henri Poincaré (B) Probabilités Et Statistiques*, Institut Henri Poincaré, 325–344. https://doi.org/10.1214/22-AIHP1242

58. Berríos S, Fenner JL, Maignan A, (2018) Simulating aggregates of bivalents in 2n= 40 mouse meiotic spermatocytes through inhomogeneous site percolation processes. *J Math Biol* 77: 1341–1362. https://doi.org/10.1007/s00285-018-1254-6

59. Cardy JL, (1984) Conformal invariance and surface critical behavior. *Nuclear Phys B* 240: 514–532. https://doi.org/10.1016/0550-3213(84)90241-4

60. Cardy J, (1998) The number of incipient spanning clusters in two-dimensional percolation. *J Phys A Math General* 31: L105–L110. https://doi.org/10.1088/0305-4470/31/5/003

61. Chae H, Yook SH, Kim Y, (2012) Explosive percolation on the Bethe lattice. *Phys Rev E* 85: 051118. https://doi.org/10.1103/PhysRevE.85.051118

62. Den Nijs M, (1979) A relation between the temperature exponents of the eight-vertex and q-state potts model. *J Phys A Math Gen* 12: 1857–1868. https://doi.org/10.1088/0305-4470/12/10/030

63. Evans LM, Sözümert E, Keenan BE, Wood CE, du Plessis A, (2023) A review of image-based simulation applications in high-value manufacturing. *Arch Comput Methods Eng* 30: 1495–1552. https://doi.org/10.1007/s11831-022-09836-2

64. Grossman T, Aharony A, (1987) Accessible external perimeters of percolation clusters. *J Phys A Math Gen* 20: L1193–L1201. https://doi.org/10.1088/0305-4470/20/17/011

65. He H, Deng H, Wang Q, Gao J, (2022) Percolation of temporal hierarchical mobility networks during COVID-19. *Philos Trans R Soc A*, 380: 20210116. https://doi.org/10.1098/rsta.2021.0116

66. Kesten H, (1987) Scaling relations for 2D-percolation. *Commun Math Phys* 109: 109–156. https://doi.org/10.1007/BF01205674

67. Montes-Orozco E, Mora-Gutiérrez RA, de-los-Cobos-Silva SG, Rincón-García EA, Gutiérrez-Andrade MA, Lara-Velázquez P, (2022) Analysis and characterization of the spread of COVID-19 in Mexico through complex networks and optimization approaches. *Complexity* 2022: 2951744. https://doi.org/10.1155/2022/2951744

68. Nienhuis B, Riedel E, Schick M, (1980) Magnetic exponents of the two-dimensional q-state Potts model. *J Phys A Math Gen*, 13: L189–L192. https://doi.org/10.1088/0305-4470/13/6/005

69. Nienhuis B, (1984) Critical behavior of two-dimensional spin models and charge asymmetry in the Coulomb gas. *J Stat Phys* 34: 731–761. https://doi.org/10.1007/BF01009437

70. Oliveira G, (2020) Early epidemic spread, percolation and Covid-19. *J Math Biol* 81: 1143–1168. https://doi.org/10.1007/s00285-020-01539-1

71. Pearson RB, (1980) Conjecture for the extended Potts model magnetic eigenvalue. *Phys Rev B* 22: 2579. https://doi.org/10.1103/PhysRevB.22.2579

72. Schramm O, (2000) Scaling limits of loop-erased random walks and uniform spanning trees. *Isr J Math* 118: 221–288. https://doi.org/10.1007/BF02803524

73. Smirnov S, Werner W, (2001) Critical exponents for two-dimensional percolation. *Math Res Lett* 8: 729–744. https://doi.org/10.4310/MRL.2001.v8.n6.a4

74. Saberi AA, (2015) Recent advances in percolation theory and its applications. *Phys Rep* 578: 1–32. https://doi.org/10.1016/j.physrep.2015.03.003

75. Torrisi GL, Garetto M, Leonardi E, (2023) Bootstrap percolation on the stochastic block model. *Bernoulli* 29: 696–724. https://doi.org/10.3150/22-BEJ1475